shot noise), and the observer's peculiar motion relative to the sources' rest frame introduces kinetic effects, such as Doppler boosting and aberration in the AGWB.

Following [580, 581], the monopole energy density of the AGWB generated by the superposition of many, unresolved, astrophysical sources can be computed by integrating the product of the energy spectrum and the source rate over the entire parameter space describing the population of GW events (see also section 4.10),

$$\bar{\Omega}_{\rm GW}(f) = \frac{f}{\rho_c c^2} \int \frac{dz}{(1+z)H(z)} R(z) \int d\vec{\theta}\, p(\vec{\theta}) \frac{dE}{df d\Omega}(f, z, \vec{\theta})\,. \tag{3.22}$$

Here, z is the redshift of the source, $\vec{\theta}$ represents the intrinsic parameters of the binary, e.g., in the case of BBH, the masses, spins and inclination angle of the orbit (i.e. the angle between the angular momentum of the binary and the direction of observation); $dE/df d\Omega$ denotes the energy spectrum per solid angle and frequency emitted by individual binaries [580, 581]. The merger rate per comoving volume $R(z)$ has been assumed here independent of the distribution of the intrinsic parameters of the binaries $p(\vec{\theta})$; see section 4.3 for a more detailed discussion of the evolution of the mass distribution with the redshift.

The other Stokes parameters of the AGWB, introduced in eq. (3.10), can be computed by replacing the energy density of the individual binaries in eq. (3.22) with an equivalent "polarized energy spectrum", which has the same amplitude as the intensity, but varies differently with respect to the inclination angle; see, e.g., [582].[9] The circular polarization of the AGWB has been discussed in the previous subsection, while cosmological models which produces polarized signals will be discussed in section 3.1.3.

The intrinsic anisotropies have been computed in [542, 543, 546–548, 583, 584] and can be classified into density anisotropies, which are related to the distribution of GW sources in the sky; Kaiser and Doppler anisotropies, which are related to the peculiar velocities of the hosts; and anisotropies imprinted by gravitational potentials along the graviton's path. A fully relativistic, gauge-invariant computation using the *cosmic rulers* formalism [585] has been performed in [547]. The monopole and anisotropies of the AGWB generated by BBH, BNS and BHNS have been fully characterized in [551, 552]. The public available code `CLASS_GWB` [552] allows computing the angular power spectrum of the intrinsic and shot noise anisotropies for different populations of CBC. The relative perturbation in the energy density of the AGWB at the observer can be written as

$$\frac{\delta\Omega^{\rm intr}_{\rm GW}}{\bar{\Omega}_{\rm GW}}(f) = \int \frac{d^3k}{(2\pi)^3} \zeta\left(\vec{k}\right) \int_0^{\eta_0} d\eta \left[\Delta^{\rm den}(\eta, k, f) + \Delta^{\rm rsd}(\eta, k, f) + \Delta^{\rm gr}(\eta, k, f)\right]\,, \tag{3.23}$$

where ζ is the primordial curvature perturbation and η_0 is the conformal time today. The expression for the source functions Δ^i can be found e.g. in [547, 552]. The cross-correlation of the intrinsic anisotropies with other LSS tracers will be discussed in section 3.4.1.2, focusing in particular on the dependence of the intrinsic anisotropies on the bias of the GWs. The intrinsic anisotropies are typically considered as Gaussian random variables of zero mean and covariance proportional to the power spectrum of the primordial curvature perturbation,

[9] Note, however, that only the Stokes parameter associated to the intensity, I, corresponds to an energy density, and no actual energy density is associated to the Stokes parameters describing linear and circular polarizations [561].

JCAP03(2026)081

although the current Planck bounds admit the possibility of the presence of a non-negligible amount of primordial non-Gaussianity in the cosmological perturbations [586]. In section 3.4.2 we will discuss the effect of primordial non-Gaussianity on the anisotropies of the AGWB in cross-correlation with the CMB.

The number of events that contribute to the AGWB fluctuate according to a Poisson distribution, inducing a shot noise term in the AGWB [561, 587–589]. In the formalism adopted here, consistently with [552, 557, 582], the shot noise of the energy density is a Gaussian random variable $\delta\Omega^{\rm SN}_{\rm GW}(\hat{n}, f)$, with zero mean and covariance given by

$$\mathcal{C}^{\rm SN}(\hat{n}, f; \hat{n}', f') = \int dz\, d\vec{\theta} \frac{R(z) p(\vec{\theta})\, \delta(\hat{n} - \hat{n}')}{(1+z)^2 H^2(z) \frac{dV}{dz d\Omega}(z) T_{\rm obs}} \prod_{\tilde{f}=f,f'} \frac{\tilde{f}}{\rho_c c^2} \frac{dE}{df d\Omega}(\tilde{f}, z, \vec{\theta})\,, \tag{3.24}$$

where we have neglected Poisson fluctuations proportional to the square of the number of GW events, suppressed by the low number of GWs per host galaxy. The term $\delta(\hat{n} - \hat{n}')$ indicates that Poisson fluctuations are uncorrelated for objects in different regions in the sky, thus the angular power spectrum is constant in the multipole space.

Kinematic anisotropies. The motion of the observer relative to the rest frame of the sources induces kinematic anisotropies in the AGWB on the order of $10^{-3}c$, consistent with measurements of Doppler boosting in the CMB [590, 591]. The velocity of the Local Group (LG) relative to the large-scale structure (LSS) generates a dipole in the anisotropies [557], while the motion of the Earth relative to the LG induces a Doppler boosting of the signal, resulting in a dipole of order one in the velocity and in a mode coupling between different multipoles, linear in both the dipole and the intrinsic anisotropies [556, 592]. In [557], a comprehensive discussion of all contributions to the dipole of the AGWB is provided, demonstrating how the Einstein Telescope (ET) in combination with the Cosmic Explorer (CE) could be used to accurately measure the velocity of the Local Group (LG), yielding results competitive with large-scale structure (LSS) observations. Ref. [558] showed that prior knowledge of the direction of the LG velocity (e.g., from CMB observations) can enhance the sensitivity to the AGWB kinematic dipole. Additionally, it showed that the Earth's peculiar motion must be accounted for to avoid biases of up to $\sim 10\%$ in the inferred dipole amplitude.

Component separation of the anisotropies. The anisotropies of the AGWB are expected to be dominated by the shot noise fluctuations, which are of the order of $10^{-1} - 10^{-3}$, because of the low number of CBC mergers in the Universe per year. Therefore, the detection of the kinetic and intrinsic anisotropies could be very challenging. Several attempts have been made in order to reduce the impact of the shot noise, for instance by cross-correlating the AGWB with galaxies [589] or lensing [551], but, because of the low angular resolution of ET to the anisotropies of the GWB, it is challenging to get a SNR larger than one for the intrinsic and kinetic components using standard techniques. In [557], it has been realized that the three contributions to the angular power spectrum exhibit different frequency dependencies for $f \gtrsim 100\,\text{Hz}$. Therefore, the distinct frequency scaling of these anisotropies could potentially be used for component separation. In the left panel of figure 21 we plot the three dipoles at different frequencies, while in the right one we show the SNR of the anisotropies with ET+CE in 5 years of observations. In the right plot, the blue line is the SNR of the kinetic

JCAP03(2026)081

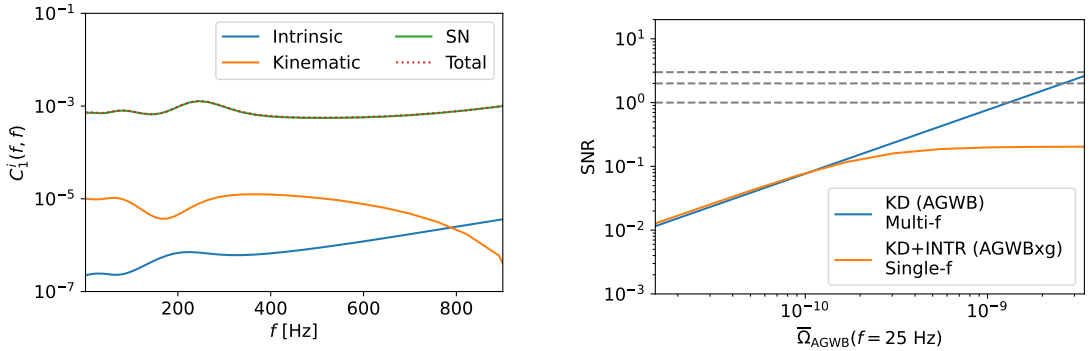

Figure 21. *Left:* plot of the intrinsic, shot noise and kinetic contributions to the dipole of the AGWB as a function of the frequency. *Right:* plot of the SNR of the kinetic dipole of the AGWB, obtained with the multi-frequency analysis of the anisotropies, and of the intrinsic and kinetic anisotropies of the AGWB, in cross-correlation with the galaxy survey SKAO2, as a function of the amplitude of the monopole of the AGWB. Here a network with the triangular ET configuration plus CE with the two interferometers (of 20km and 40km) placed in Hanford and Livingston for 5 yrs has been considered.

dipole of the AGWB with the multi-frequency analysis. When the instrumental noise is taken into account, it becomes evident that a kinetic dipole in an AGWB with an amplitude consistent with the current LVK bound could be detected with an SNR $\simeq 3$. In order to show the power of the multi-frequency analysis, we also plot the SNR of the intrinsic and kinetic anisotropies of the auto- and cross-correlation of the AGWB with the SKAO2 galaxy catalogue [593], up to $\ell_{\rm max} = 100$ (orange line), without considering the frequency dependence of the anisotropies. When instrumental noise does not dominate the AGWB signal, it become evident that multi-frequency analysis seems to be the most efficient technique for addressing the shot noise issue, improving by orders of magnitude the SNR.

3.1.3 Polarization of the GWB and parity violation

3.1.3.1 Polarization of the AGWB. In GR, the AGWB is expected to be unpolarized because the average over polarization angles set to zero linear polarizations and the average over inclination angles set to zero the circular polarization (see [561] for the explicit computation). However, because of the effect of sampling a realization, shot noise can generate a net amount of both linear and circular polarization (even for isotropic source distributions [561]). In particular, circular polarization could be observed by ET+CE with an SNR greater than 2 in one year of observations [582]. A computation analogous to eq. (3.24) for the V Stokes parameter indicates that the amplitude of the circular polarization is indeed comparable to the shot noise in the intensity and exhibits an angular power spectrum that is constant in multipole space. In the right panel of figure 20 we plot the monopole (intensity) and amplitude of the shot noise as a function of frequency, along with the PLS of the intensity (monopole) and circular polarization (monopole plus anisotropies). The circular polarization of the AGWB represents a foreground for the detection of polarized cosmological signals, and component separation techniques based on the frequency and angular dependence of the signal should be adopted [582].

JCAP03(2026)081

Various mechanisms in the early Universe can generate parity violation, leading to an uneven production of left- and right-handed circularly-polarized GWs. Since parity-violating GWs are expected to be cosmologically sourced, polarization could be used together with the intensity to identify the primordial origin of the signal, although the circular polarization of the AGWB discussed is an unavoidable foreground for polarized cosmological backgrounds. Searches for polarized GWBs can allow one to place constraints on parity-violating theories, as we discuss next.

3.1.3.2 Chiral GW Sources. A number of mechanisms can result in parity violation in the early Universe [594]. Two compelling, well-studied, classes of parity-violating inflationary models that could lead to a circularly polarized GW background include Chern-Simons gravity [595–598], and axion-gauge field inflation [599–623]. More details on axion inflation mechanism can be found in section 3.2.1.2. Other sources such as GWB from turbulence in the primordial plasma induced either from cosmological first-order (electroweak or QCD phase transition beyond the Standard Model) phase transitions [624–626] and from the primordial magnetic fields that are coupled to the cosmological plasma [627–631] can be chiral. Although an AGWB is typically expected to be unpolarized, polarization can occur when considering shot noise fluctuations, as we discussed in section 3.1.2.2.

3.1.3.3 Detection Formalism for Chiral Gravitational Waves. We now discuss the formalism used in detecting parity-violating backgrounds, following [560, 632]. This formalism was used in practice in the LVK data in [633, 634], and in simulated third-generation networks in [633, 635]. We use the circularly polarized bases $e^R = (e^+ + ie^\times)/\sqrt{2}$ and $e^L = (e^+ - ie^\times)/\sqrt{2}$ (with $+$ and $\times$ the plus and cross polarizations, respectively) to obtain the right- and left-handed modes $h_R = (h_+ - ih_\times)/\sqrt{2}$ and $h_L = (h_+ + ih_\times)/\sqrt{2}$, respectively. Using eq. (3.10), the right-right and left-left correlators can then be written as

$$\begin{pmatrix} \langle h_R^*(f,\hat{\mathbf{n}}) h_R(f',\hat{\mathbf{n}}')\rangle \\ \langle h_L^*(f,\hat{\mathbf{n}}) h_L(f',\hat{\mathbf{n}}')\rangle \end{pmatrix} = \frac{1}{8\pi}\delta(f-f')\delta(\hat{\mathbf{n}},\hat{\mathbf{n}}') \begin{pmatrix} I(f,\hat{\mathbf{n}}) - V(f,\hat{\mathbf{n}}) \\ I(f,\hat{\mathbf{n}}) + V(f,\hat{\mathbf{n}}) \end{pmatrix}, \tag{3.25}$$

We use the standard cross-correlation estimator [80, 636–638]

$$\begin{aligned} \langle \hat{C}_{d_1 d_2}\rangle &= \int_{-\infty}^{\infty} df \int_{-\infty}^{\infty} df' \delta_T(f-f')\langle s_{d_1}^*(f) s_{d_2}(f')\rangle \tilde{Q}(f') \\ &= \frac{3H_0^2 T}{10\pi^2}\int_0^{\infty} df \frac{\Omega'_{\rm GW}(f)\gamma_I^{d_1 d_2}(f)\tilde{Q}(f)}{f^3}, \end{aligned} \tag{3.26}$$

where

$$\begin{aligned} \Omega'_{\rm GW} &= \Omega_{\rm GW}\left[1 + \Pi(f)\frac{\gamma_V^{d_1 d_2}(f)}{\gamma_I^{d_1 d_2}(f)}\right], \\ \gamma_I^{d_1 d_2}(f) &= \frac{5}{8\pi}\int d\hat{\Omega}(F_{d_1}^+ F_{d_2}^{+*} + F_{d_1}^\times F_{d_2}^{\times *}) e^{2\pi i f \hat{\Omega}\cdot\Delta\vec{x}}, \\ \gamma_V^{d_1 d_2}(f) &= -\frac{5}{8\pi}\int d\hat{\Omega}(F_{d_1}^+ F_{d_2}^{\times *} - F_{d_1}^\times F_{d_2}^{+*}) e^{2\pi i f \hat{\Omega}\cdot\Delta\vec{x}}, \end{aligned} \tag{3.27}$$

with H_0 the Hubble parameter, T the observing time, $\delta_T(f) = \sin(\pi f T)/(\pi f)$, $\tilde{s}_{d_1}(f)$ and $\tilde{s}_{d_2}(f)$ the Fourier transforms of the strain time series of two GW detectors (denoted by

JCAP03(2026)081

d_1, d_2). We apply the usual $\tilde{Q}(f)$ as the optimal filter taking into account detectors' strain power spectral densities, and $F_n^A = e_{ab}^A d_n^{ab}$ stands for the contraction of the tensor modes of polarization A to the nth detector's geometry. We denote by $\gamma_I^{d_1 d_2}$ the standard overlap reduction function of two detectors d_1, d_2, and by $\gamma_V^{d_1 d_2}$ the overlap function associated with the parity violation term. The polarization degree, $\Pi(f) = V(f)/I(f)$, takes on values between -1 (fully left polarization) and 1 (fully right polarization), with $\Pi = 0$ being an unpolarized isotropic GWB. We build the Gaussian log-likelihood for a network of N detectors

$$\log p(\hat{C}(f)|\boldsymbol{\theta}) \propto \sum_{i,j>i}^{N} \sum_{f} \frac{\left[\hat{C}_{d_i d_j}(f) - \Omega'_{\rm GW}(f, \boldsymbol{\theta})\right]^2}{\sigma^2_{d_i d_j}(f)}, \tag{3.28}$$

where $\hat{C}_{d_i d_j}(f)$ is the frequency-dependent cross-correlation estimator of the GWB calculated using data from detectors d_i, d_j, and $\sigma^2_{d_i d_j}(f)$ is its variance, and $\boldsymbol{\theta}$ are the associated parameters to the tested GWB model.

3.1.3.4 Detection Prospects for Chiral Gravitational Waves. In the context of ET, this formalism has a number of ramifications on parity violation detection. We plot the standard and parity-violating associated overlap reduction functions in figure 22. One can see that the parity violating associated overlap reduction function between two detectors of an assumed triangular design[10] would be approximately 0 due to their co-planarity to one another. From eq. (3.27) this would imply that $\Omega_{\rm GW} \approx \Omega'_{\rm GW}$ for even entirely chiral GWs. Thus, parity- violation inferences on GW data with this formalism is difficult with a triangular ET configuration alone. However, ET in combination with other detectors (such as CE) should have $\gamma_V^{d_1 d_2}(f) \neq 0$ due to their non-coplanarity — thus allowing for parity violating inferences in extended networks whilst taking advantage of ET's sensitivity. A 2L design for ET, and any additional detectors in the network, would not face such problems for similar reasons. Reconsidering the previously described formalism while taking into account the full response functions and noise curves across the entire frequency band (for planar detectors), it is found that $\mathcal{O}(1)$ net polarization can be detected in the GWB, with a magnitude of $h^2\Omega_{\rm GW} \simeq 10^{-11}$ and an SNR of order one [639]. Fully analytical and covariant details of these parity-sensitive response functions, which are critical for parity violation detection, can be found in [639]. Extensions to search for GWBs with anisotropies and circular polarization have been developed and studied in the context of ground-based detectors [640]. Many results are in agreement with [634] in an LVK context; however, an ET+CE network can improve this by about three orders of magnitude. As discussed in section 3.1.2.2, the presence of a circularly polarized AGWB may provide an additional challenge for CGWB parity violation detection [582]. A simplified example showed that, by taking advantage of different background features, such as their frequency dependence and features in the sky maps, it

[10] We follow the terminology of the 2020 ET Design Report Update, https://apps.et-gw.eu/tds/?r=18715: the high-frequency (HF) and low-frequency (LF) interferometers that make the so-called "xylophone" configuration are indeed referred to as "interferometers". The combination of a HF interferometer and a LF interferometer (whether in a L-shaped geometry, or with arms at 60° as in the triangle configuration) is called a "detector". The whole ensemble of detectors is called an "observatory". So, ET in the triangle configuration is made of three detectors for a total of six interferometers, while in the 2L configuration it is made of two detectors, for a total of four interferometers.

JCAP03(2026)081

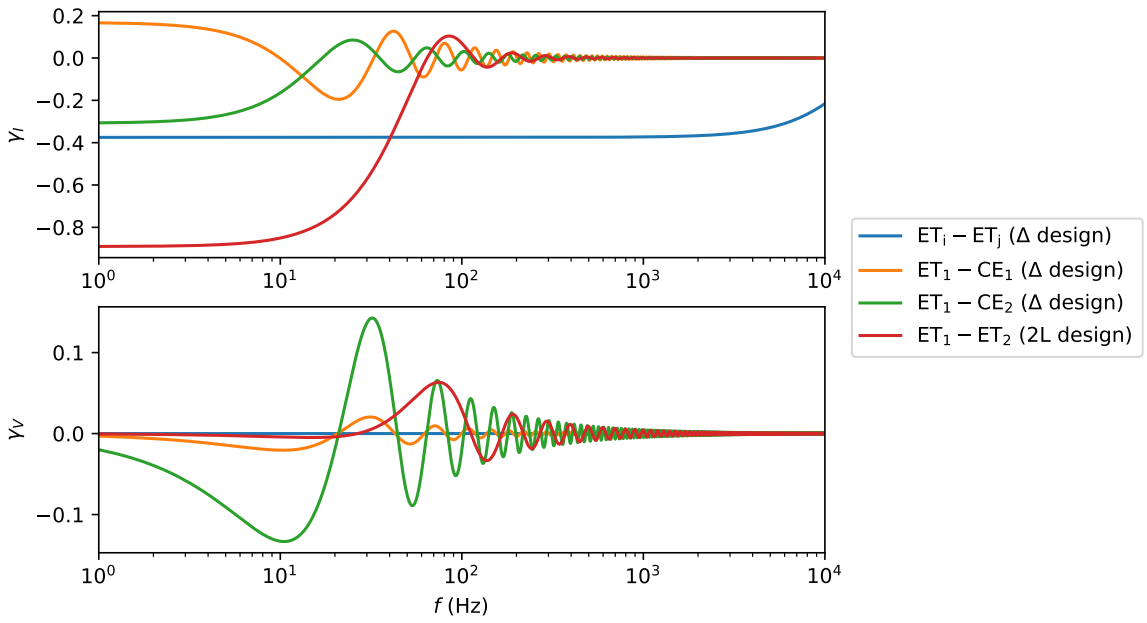

Figure 22. Standard and parity-violating overlap reduction functions plotted over ground-based detector frequency range. When assuming a triangular configuration for ET, we plot the result for a pair of ET detectors (out of the three composing the triangle), and for one ET detector (out of the three composing the triangle) and a Cosmic Explorer (CE), with CE taken either in the current Hanford site or in the current Livingston sites. When assuming the 2L configuration for ET, we plot the result for this pair of L-shaped detectors. The triangular ET design is assumed in Virgo location. We denote the triangular pairing with i, j as all pairings produce the same overlap reduction functions.

is possible to reconstruct the primordial background with good precision using ET+CE, primarily limited by instrumental noise, as in the case of the intensity. That said, separation corrections of the order of 20% to the total SNR must be carefully taken into account.

3.1.4 Source separability

Once a GWB is detected, the next important question will be to relate the signal to the sources that contribute to it. In particular, one will be interested in separating compact binary coalescences (namely a pure astrophysical contribution) from possible sources of a cosmological origin (for instance inflation, cosmic strings or first-order phase transitions). A Bayesian analysis has shown that current terrestrial interferometers (i.e., Advanced LIGO and Advanced Virgo network), even once operating at design sensitivity will not allow for separation of the sources [641]. Assuming one is able to do an individual source subtraction [642], the residual CBC contribution to the GWB will be dominated by unresolved binary neutron star mergers at the level of $\sim 10^{-11}$ at 10 Hz.[11] Third generation (3G) detectors, like Einstein Telescope, and in particular a network of 3G detectors will allow simultaneous separation of astrophysical and cosmological GWBs, provided reasonable levels of individual source subtraction can be achieved [641].

[11] A more detailed analysis shows that the result actually depends on the shape of the cosmological spectrum that is being searched, see [643] and section 10.5.3.

JCAP03(2026)081

The separability of sources in the ET frequency band has several challenges given that multiple components contribute to the overall signal. This makes the parameter space large and complex. This complexity, along with degenerate characteristics, complicates such a task making it also computationally challenging. A computationally less demanding approach could be performed in a two-step process: first, reconstruct the GWB spectrum agnostically (as in LISA data analysis techniques [644–647]); second, convert the spectrum constraints into population and cosmological parameter constraints (see e.g., [648] for a recent application). This method allows to balance accuracy and feasibility and can help identify relevant parameter spaces for full Bayesian techniques.

Another limitation in the detection of the GWB signal is the impact of significant residuals, primarily from uncertainties in coalescence phase and luminosity distance, when resolved sources are subtracted [642, 643]. Enhanced signal subtraction methods are necessary to improve the observation of other astrophysical and cosmological GWBs.

3.1.5 Impact of correlated noise on GWB

To be able to resolve the weak signal from the GWB, one needs to rely on cross-correlation methods to suppress independent noise sources at the different detectors. In the absence of correlated noise, this implies that any remaining correlated signal is from GWs. However, past research has shown that such a correlation analysis is prone to noise contamination from correlated noise sources, both for co-located as well as widely separated detectors. As a first order approach one should consider to reduce the noise couplings, so to lower or entirely remove such correlated noise disturbances. If this is deemed impossible one could consider performing a joint parameter estimation taking both the correlated noise and the GWB signal into account (see section 3.1.6). Finally, if the correlated noise has a much larger amplitude and/or is not known with high accuracy, one has to consider whether it is more efficient to remove all the contaminated frequency bins/time segments and only use the part of the data with the highest data quality.

In the next sections we will discuss two noise sources, which have been considered to potentially contaminate the search for an isotropic GWB with the ET. Here we only focus on fundamental, environmental noise sources and their impact. Earlier work has indicated that co-located detectors could have additional correlated noise from detector infrastructure, which could potentially have significantly higher effects [649]. However, more work is needed to understand the levels of correlation of infrastructural noise in a realistic ET environment.

3.1.5.1 Noise correlations from electromagnetic phenomena. On the Earth, every second about hundred lightning strikes occur. This vast amount of electromagnetic discharges creates standing waves in the cavity formed by the Earth's surface and the ionosphere, known as the Schumann resonances [650, 651]. With the fundamental mode and subsequent harmonics occurring at $\sim$7.8 Hz, $\sim$14 Hz, $\sim$ 21Hz, etc., this broadband noise source falls within ET's low frequency sensitivity range. Due to the global nature of this noise source, it has the potential to couple coherently to GW interferometric detectors, no matter their separation. In past work the Schumann resonances were coherently observed in the magnetometers at both the LIGO sites as well as at Virgo [652–656].

JCAP03(2026)081

Earlier work has highlighted how correlations due to electromagnetic fluctuations can impact the search for an isotropic SGWB up to $\sim 30\,\mathrm{Hz}$ if one assumes similar levels of magnetic coupling at the ET compared to 2G detectors such as LIGO and Virgo [649]. The coupling should be reduced by three to four orders of magnitude per detector around 5 Hz to remove any noise contamination [649]. Furthermore, above 30 Hz there is potential of additional contamination in narrow frequency bands around resonant features in the magnetic coupling. More work is needed to understand whether the magnetic coupling to ET can be reduced compered to 2G detectors to (partially) deal with this noise contamination. Also the effectiveness of noise subtraction, as described in [653–655], or joint estimation, as discussed in [657], in case of such a loud noise sources should be further investigated. However, it is to be noted the correlated signal from magnetic origin has a steeply declining behavior as a function of frequency, whereas many of the expected GW backgrounds have a flat or slowly increasing Ω_{GW} signature. This characteristic behavior originates from the steeply declining magnetic coupling function observed at 2G detectors.

3.1.5.2 Noise correlations from seismic phenomena. More recent work has also investigated the effect of coherent seismic noise and the subsequent Newtonian Noise (NN) [658, 659].[12] This noise source will only appear correlated between different ET detectors if they are located close to each other. In this context, the detectors are considered to be located close to each other if their input and/or end towers are separated by a distance of several hundreds of meters up to several kilometers. This will be the case for ET in the triangular configuration. The exact distance at which the coherence of seismic noise decreases enough in the relevant frequency band for the ET is likely to be somewhere between 2 km and 10 km; however, additional research is needed to confirm this.

Depending on the specific seismic environment of ET's site, the coherent NN noise originating from seismic body-waves will contaminate the sensitivity to an isotropic SGWB up to 20 Hz–40 Hz [658, 659], as shown in figure 23. Similar to the magnetic noise scenario, the lowest frequencies are affected more seriously and the NN is predicted to have a declining behavior as a function of frequency (when expressed in terms of Ω_{GW}). This might facilitate spectral separation if one is looking for a GWB which has a flat or increasing Ω_{GW} spectrum as function of frequency. In section 3.1.6 we will discuss the recovery of a cosmological signal in the presence of such correlated noise.

3.1.6 Reconstruction of GWBs in presence of correlated noise

As discussed in section 3.1.5, a critical challenge in detecting the GWB is the precise characterization of correlated detector noise, which is essential for distinguishing the signal from spurious instrumental and environmental fluctuations. We have seen that the triangular geometry suffers from correlated noise due to the relative proximity of interferometer components, leading to potential contamination in GWB searches.

The effect of correlated noise on the detection and characterization of the GWB with ET has been recently studied in [660], where a Bayesian framework has been introduced

[12] NN is a force directly exerted on GW test-masses caused by density fluctuations in the surrounding medium.

JCAP03(2026)081

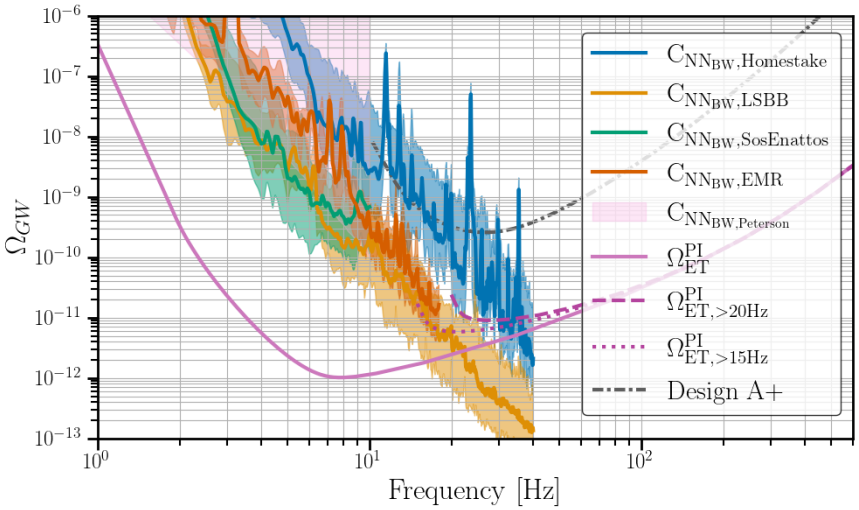

Figure 23. The projected impact from correlated NN from body-waves on the search for an isotropic GWB. We present budget based on observed seimic correlations from four different seismic sites. Note that many parameters, such as depth, horizontal separation, etc., vary for the different sites; see [659] for an in-depth discussion. Reprinted figure with permission from [659], Copyright (2024) by the American Physical Society.

to simultaneously reconstruct the parameters of the GWB and the correlated noise, both modeled as power laws in the frequency domain. For detectors I and J, the covariance of the noise is defined as the two-point correlation function, $N_{IJ}(f) \equiv \langle \tilde{n}_I(f)\tilde{n}^*_J(f')\rangle$. For the triangle configuration, in ref. [660] is made the assumption that all diagonal terms in the PSD are given by the same function $N_d(f)$, and that all off-diagonal terms are also all given by the same function $N_o(f)$, so that

$$N_{IJ}(f) = \begin{pmatrix} N_d(f) & N_o(f) & N_o(f) \\ N_o(f) & N_d(f) & N_o(f) \\ N_o(f) & N_o(f) & N_d(f) \end{pmatrix} , \tag{3.29}$$

and it is assumed that the off-diagonal terms can be parametrized by a simple power-law

$$N_o(f) = N_o(2.75\,\mathrm{Hz}) \left(\frac{f}{2.75\,\mathrm{Hz}}\right)^{n_{\mathrm{noise}}} . \tag{3.30}$$

Defining $r = N_o(2.75\,\mathrm{Hz})/N_d(2.75\,\mathrm{Hz})$, so that r is the correlation coefficient at the reference frequency $2.75\,\mathrm{Hz}$, we then write

$$N_o(f) = N_d(2.75\,\mathrm{Hz})\, r \left(\frac{f}{2.75\,\mathrm{Hz}}\right)^{n_{\mathrm{noise}}} , \tag{3.31}$$

The value of the tilt expected from Newtonian noise is $n_{\mathrm{noise}} = -8$ [658, 659, 661], while different values of the correlation coefficients, in the physical range $r \in [-0.5, 1]$, have been tested.

JCAP03(2026)081

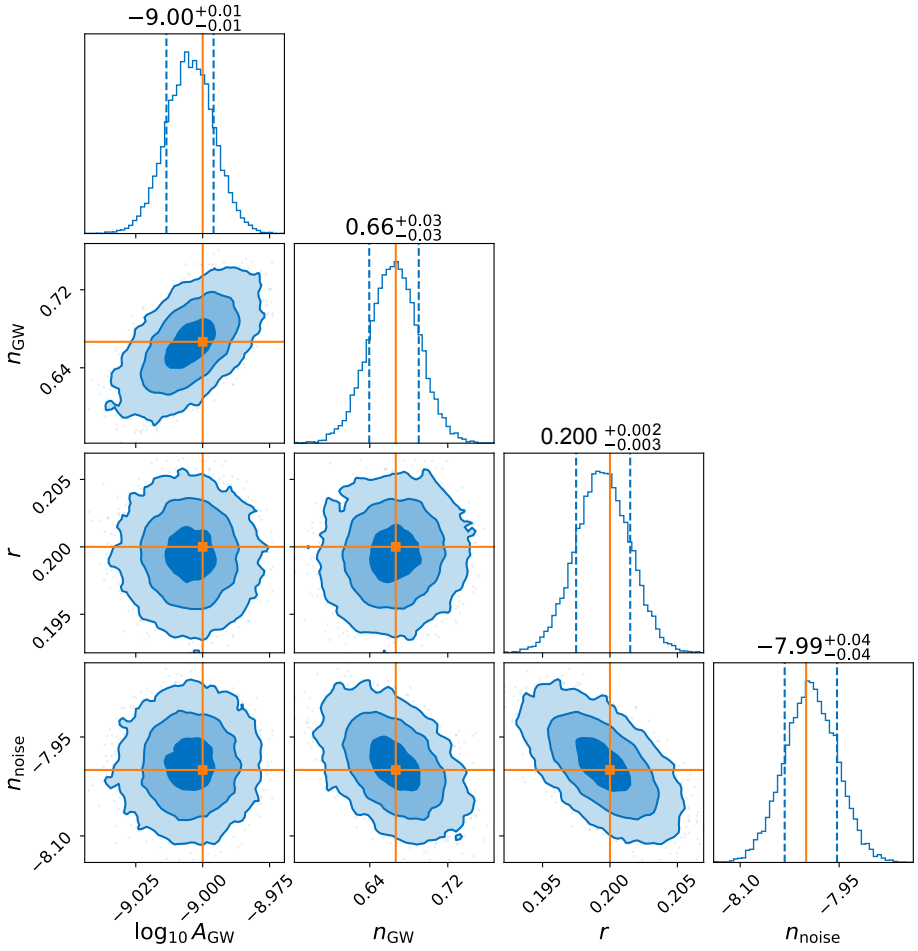

Figure 24. Corner plot of the posterior distributions for the log-amplitude and tilt of the GWB, $\{\log_{10} A_{\rm GW}, n_{\rm GW}\}$ for the correlation coefficient and tilt of the noise, $\{r, n_{\rm noise}\}$, when the injected signal has $\log_{10} A_{\rm GW} = -9$ and $n_{\rm GW} = 2/3$, while the injected noise has $r^{\rm inj} = 0.2$, $n_{\rm noise} = -8$. The shaded areas represent the 1-, 2-, and 3-σ credible regions. The orange lines indicate the injected values for the four parameters. Reproduced with permission from [660].

The stochastic GW signal is also modeled as a simple power-law,[13]

$$\Omega_{\rm GW}(f) = A_{\rm GW} \left(\frac{f}{25\,{\rm Hz}}\right)^{n_{\rm GW}} \tag{3.32}$$

Under these assumptions, ref. [660] derives a general likelihood for the GWB that accounts for correlated noise and performs parameter estimation for the whole set of parameters $\{A_{\rm GW}, n_{\rm GW}, r, n_{\rm noise}\}$ that characterize the signal and the correlated noise.

The quality of the reconstruction depends, of course, on the amplitude of signal with respect to the noise. Figure 24 shows the result of the parameter reconstruction when the

[13]For the GW signal, it is customary to take a reference frequency closer to the minimum of the PLS, such as 25 Hz here, while for the correlated noise in eq. (3.31) is used a reference frequency 2.75 Hz closer to the region where it is more relevant. Of course, different choices of the reference frequency can be reabsorbed into different definitions of the corresponding amplitudes.

JCAP03(2026)081

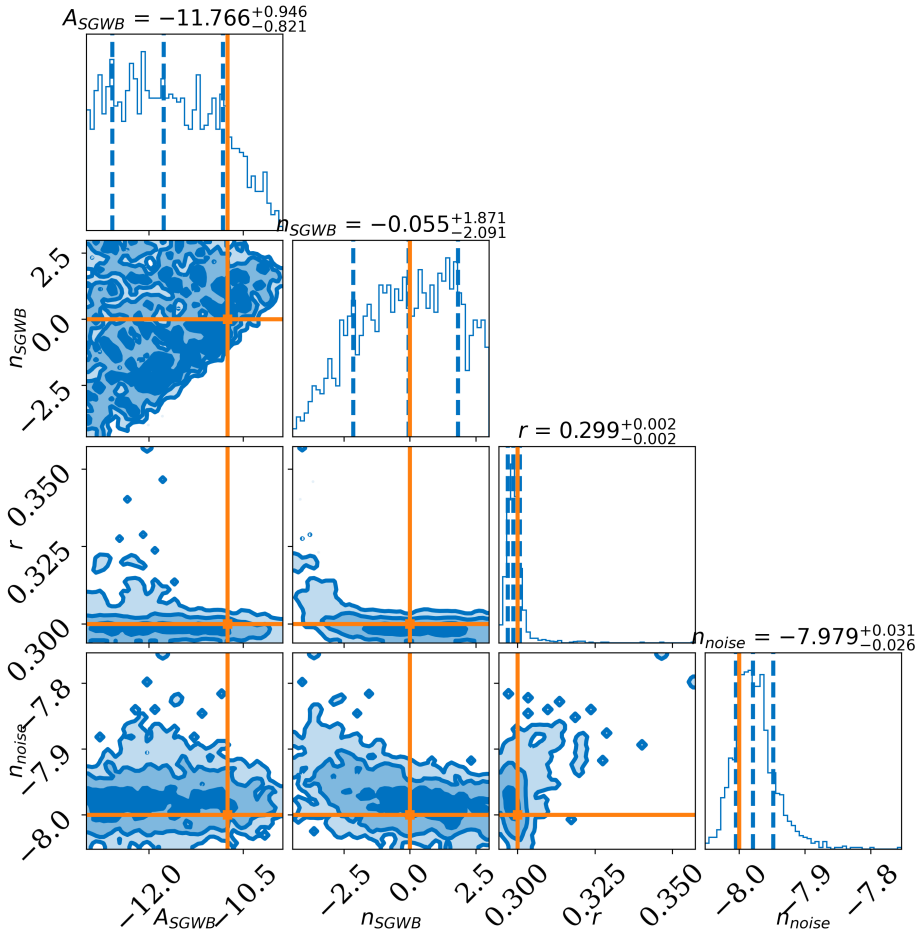

Figure 25. As in figure 24 when the injected signal has $\log_{10} A_{\rm GW} = -11$ and $n_{\rm GW} = 0$, while the injected noise has $r^{\rm inj} = 0.2$, $n_{\rm noise} = -8$.

injected correlated noise has the correlation coefficient $r^{\rm inj} = 0.2$ and a tilt $n^{\rm inj}_{\rm noise} = -8$, while the injected GW signal is taken to have $A^{\rm inj}_{\rm GW} = 10^{-9}$, $n^{\rm inj}_{\rm GW} = 2/3$, which are the amplitude and tilt expected for the stochastic background generated by the superposition of coalescing binaries in the inspiral phase (see figure 205). This injected stochastic GW background accumulates an SNR of about 67 in just 1 day of observation (restricting the analysis to frequencies below 200 Hz, where the CBC background can be modeled as a power law with $n^{\rm inj}_{\rm GW} = 2/3$), while the correlated noise, if interpreted as a signal, has SNR ~ 135 (again for 1 day of observation).[14] Since the SNR for a two-detector (or multiple-detector) correlation grows with the integration time as $T^{1/2}$, see eq. (10.59), these spectra correspond to an SNR of about 1280 and 2580, respectively, for 1 yr of integration.

In this case, where the GW signal has a very large SNR and a mild blue slope, quite different from the steep red slope of the noise, we see from the figure that, already with

[14]These are the signal-to-noise ratio computed using only the diagonal term N_d for the noise, i.e. we are considering the off-diagonal term as a competing correlated signal.

JCAP03(2026)081

one day of observation, both the GWB and noise parameters could be reconstructed with percent-level accuracy.

We have repeated the analysis for a GW background with $A_{\rm GW}^{\rm inj} = 10^{-11}$, $n_{\rm GW}^{\rm inj} = 0$. Such a background would produce a signal-to-noise ratio SNR = 3 in 1 day of observation (i.e., SNR $\simeq$ 57 in 1 yr). For the noise we still take $r^{\rm inj} = 0.2$ and a tilt $n_{\rm noise}^{\rm inj} = -8$. The results of the parameter reconstruction with 1 day of data are shown in figure 25. We see that in this case the quality of reconstruction of the signal is less good (and in particular the tilt cannot be reconstructed), as expected from the fact that it has a smaller SNR, while the parameters of the noise, which is the same as before and therefore has a very large SNR (again, about 135 in just 1 day), can still be reconstructed well. Note that this reconstruction is obtained from just 1 day of data, but this is due to the fact that also the injected GW signal reaches an SNR equal to 3 in just 1 day. The effect of the same correlated noise will be significantly more important in the reconstruction of GW backgrounds with even lower amplitude, such as a background that would accumulate, say, SNR = 3 in 1 yr of data, i.e. near the nominal sensitivity limit determined by the diagonal terms in eq. (3.29).

This shows that the presence of correlated noise in the triangle configuration is a relevant limitation, although it could still possible to reconstruct the GWB parameters, provided that the SNR of the signal is sufficiently large and that a reliable noise model is available. This conclusion, however, holds when the injected data are generated using the same power-law noise model that is then employed in the recovery of the signal. When dealing with real data, more sophisticated noise models, possibly informed by seismographic data taken on-site, will be necessary to achieve the required level of precision in noise reconstruction. The 2L configuration, where correlated noise is (to a first approximation) negligible, is immune to this problem.

3.2 Probing the early Universe

3.2.1 GWs from inflation

3.2.1.1 The single-field slow-roll paradigm: vacuum fluctuations. In its simplest realization, inflation is driven by a single scalar field slowly rolling down its potential [662–665]. There exist several such "minimal" inflationary models that fare well compared to observations, such as the Starobinsky model [663] or Higgs inflation [666]. The general prediction associated with single-field slow-roll models is that of a slightly red-tilted GW spectrum sourced by vacuum fluctuations [667, 668]. Typically, CMB probes are then expected to provide the most stringent constraints on this class of inflationary models.

Let us recall that, in a generic inflationary model, the primordial spectrum of tensor perturbations $\mathcal{P}_{T,\rm in}(k)$ is defined by[15]

$$\langle h_{ij}^{\rm TT}(\eta_{\rm in}, \mathbf{x}) h_{ij}^{\rm TT}(\eta_{\rm in}, \mathbf{x})\rangle = \int_0^\infty \frac{dk}{k}\, \mathcal{P}_{T,\rm in}(k)\,, \tag{3.33}$$

where $\eta_{\rm in}$ is chosen deep into radiation dominance, and such that all modes of interested are super-horizon, and is taken as the initial value of conformal time for the subsequent

[15] We follow the definitions and notation of chapter 19 of [60].

JCAP03(2026)081

evolution until the present epoch. A useful parametrization for the primordial GW spectrum in single-field slow-roll (SFSR) models is a power law

$$\mathcal{P}_{T,\mathrm{in}}(k) = A_T(k_*) \left(\frac{k}{k_*}\right)^{n_T} , \tag{3.34}$$

where k_* is a suitably chosen pivot scale (for CMB studies typical values are $k_* = 0.05\,\mathrm{Mpc}^{-1}$, or $k_* = 0.002\,\mathrm{Mpc}^{-1}$), while n_T is the tensor spectral index, which in general is a function of k. In similar way, can be parameterized the primordial scalar power spectrum, with an amplitude $A_{\mathcal{R}}(k)$, where $\mathcal{R}$ is the primordial curvature perturbation. Using the equivalent notation $A_S(k) \equiv A_{\mathcal{R}}(k)$ for the amplitude of scalar perturbations, the ratio of the amplitude of the tensor and scalar power spectra allows to define the tensor-to-scalar ratio $r(k) = A_T(k)/A_S(k)$.

In the SFSR paradigm, for $f \gtrsim 10^{-4}\,\mathrm{Hz}$ (and therefore at the frequencies relevant for ground-based detectors, as well as for LISA and even PTA) the GWB produced by the amplification of quantum vacuum fluctuations can then be written as

$$h_0^2\Omega_{\mathrm{gw}}(f) \simeq 1.44 \times 10^{-16} \left(\frac{r(k_*)}{0.1}\right) \left(\frac{A_S(k_*)}{2.14 \times 10^{-9}}\right) \left(\frac{f}{f_*}\right)^{n_T} \left(\frac{106.75}{g_*(T_k)}\right)^{1/3} , \tag{3.35}$$

(see, e.g., eq. (21.357) of [60]).[16] CMB observations constrain the amplitude of scalar perturbations to $A_S(k_*) \simeq 2.14 \times 10^{-9}$ at a pivot scale $k_* = 0.05\,\mathrm{Mpc}^{-1}$, and put an upper bound on $r(k_*)$ of about 0.03, when the consistency relation $r = -8n_t$ is assumed [669](see also [670] for a constrain at $k_* = 0.01$). If the consistency relation is not assumed the bounds are less stringent with $r_{0.01} < 0.066$ and $-0.76 < n_T < 0.52$ at 95%CL [671]. The frequency f_* corresponding to the pivot scale k_* is extremely low, compared to the frequencies explored by ground-based detectors. For instance, a pivot scale $k_* = 0.002\,\mathrm{Mpc}^{-1}$ corresponds to $f_* \simeq 3 \times 10^{-18}\,\mathrm{Hz}$. Therefore, in eq. (3.35), at the frequencies of ground-based detectors (or of LISA), in the term $(f/f_*)^{n_T}$, the factor f/f_* is very large, and the prediction for $h_0^2\Omega_{\mathrm{gw}}(f)$ at frequencies relevant for ET depends crucially on the sign of n_T. For single-field slow-roll models of inflation, $n_T = -r(k_*)/8$, so the tilt is negative (and small in absolute value, given the observational bound $r(k_*) < 0.1$). Then, at the frequencies relevant for ET, $h_0^2\Omega_{\mathrm{gw}}(f)$ is below 10^{-16}, and is not detectable by 3G detectors, see figure 26.

3.2.1.2 Multi-field scenarios. Remarkably, there exist a non-trivial number of multi-field inflationary scenarios supporting a detectable signal at interferometer scales. Amongst these, a promising class of models that has gained considerable attention is axion inflation (see [672] for a review). In these models the axion potential has an (approximate) shift symmetry protecting its light mass from large quantum fluctuations. When the axion-like particle plays the role of the inflaton the symmetries of the theory addresses directly the η-problem. Well studied single-field realisation of axion inflation (such as natural inflation [673]) have been recently ruled out [674]. Remarkably, multi-field realizations exist [599–623, 675, 676] with intriguing gravitational wave phenomenology and the added feature of a sub-Planckian axion decay constant, a very desirable feature from the top-down perspective [677]. In

[16] The expression of $h_0^2\Omega_{\mathrm{gw}}(f)$ for $f_{\mathrm{eq}} \lesssim f \lesssim 10^{-4}\,\mathrm{Hz}$, where $f_{\mathrm{eq}} \simeq 3 \times 10^{-17}\,\mathrm{Hz}$, is also quite similar, see eq. (19.291) of [60].

JCAP03(2026)081

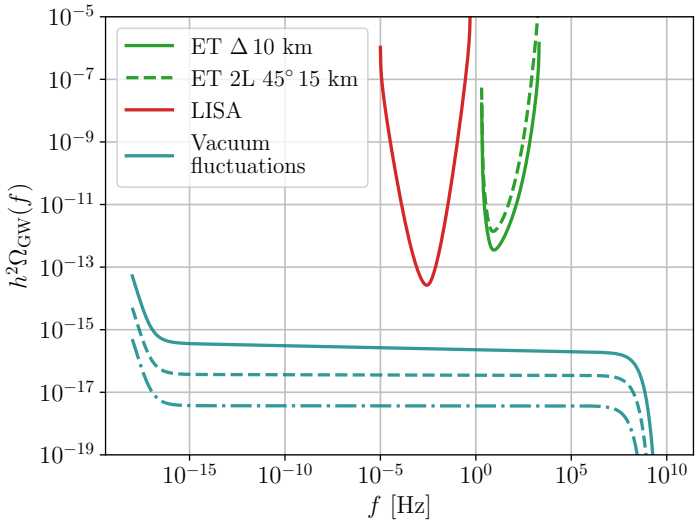

Figure 26. Spectrum of the single-field slow-roll inflation as a function of frequency, together with the PLS of LISA and ET in two different configurations. The solid, dashed, dot-dashed standard inflation curves are computed by adopting $r(k_\star) = 0.1$, $r(k_\star) = 0.01$ and $r(k_\star) = 0.001$, respectively.

multi-field constructions the axion is typically coupled to a (hidden) gauge sector via a Chern-Simons term. Note that models with multiple axion-like particles (ALPs) have also been explored [678, 679], with ALPs populating also spectator sectors of the inflationary Lagrangian. The GW signatures of theories rich in spectator fields are very similar to those of their more minimal counterparts.

Let us consider the example of a pseudo-scalar inflaton field ϕ and $\mathcal{N}$ gauge fields A^I_μ (see e.g. [599–601, 603, 604, 675, 680, 681]):

$$\mathcal{L} = -\frac{1}{2}\partial_\mu\phi\partial^\mu\phi - \frac{1}{4}F^I_{\mu\nu}F_I^{\mu\nu} - V(\phi) - \frac{\lambda^I}{4f}\phi F^I_{\mu\nu}\tilde{F}_I^{\mu\nu}\,, \tag{3.36}$$

with scalar potential V typically of the natural inflation type $V(\phi) = \Lambda^4[1+\cos(\phi/f)]$, and where $F^{I\,a}_{\mu\nu} = \partial_\mu A^{I\,a}_\nu - \partial_\nu A^{I\,a}_\mu - g\,\epsilon^{abc}A^{I\,b}_\mu A^{I\,c}_\nu$ is the field strength tensor. Notice that the gauge group index "a" is suppressed in eq. (3.36). The field strength reduces to the Abelian case for vanishing g. The dual field strength tensor is $\tilde{F}_I^{\mu\nu} = \epsilon^{\mu\nu\alpha\beta}F^I_{\alpha\beta}/(2\sqrt{-g})$ and f is the mass scale suppressing higher dimensional operators, whilst λ parameterizes the strength of the Chern-Simons coupling. This setup leads to exponential gauge boson production, with potentially detectable GWs and possibly amplified scalar perturbation sourced by the gauge field.

Common to Abelian and non-Abelian scenarios is the following dynamics: the axion-inflaton rolls down its potential and dissipates some of its kinetic energy into the gauge sector. The parity-violating nature of the Chern-Simons term results in only one polarisation of the gauge fields being amplified when sourcing GWs (and scalar fluctuations). Such a sourcing mechanism may give rise to a blue or bump-like features in the GW and scalar spectra depending also on the inflaton/spectator role played by the axion(s).

JCAP03(2026)081

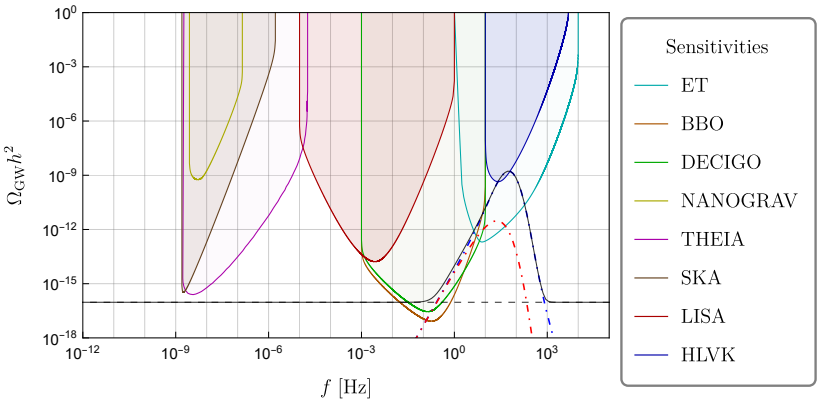

Figure 27. The GW density $\Omega_{\rm GW}$ obtained in the case of a spectator axion superimposed with the sensitivity curves of GW detectors, including ET. The blue (red) dashed line corresponds to the strongly (weakly) amplified polarization. The continuous black line gives the total signal.

The corresponding GWB can be characterised as [601, 614, 682]

$$\Omega_{\rm GW} \simeq \begin{cases} \frac{1}{12}\Omega_{R,0}\left(\frac{H^2}{\pi^2 M_{\rm Pl}^2}\right)\left(1+4.3\times10^{-7}\frac{H^2}{M_{\rm Pl}^2\xi^6}e^{4\pi\xi}\right), & \text{for } U(1) \\ \frac{1}{12}\Omega_{R,0}\left(\frac{H^2}{\pi^2 M_{\rm Pl}^2}\right)_{\xi=\xi_{\rm cr}}\left[1+\frac{1}{2}\xi_{\rm cr}^6\left(\frac{2^{7/4}H}{g\sqrt{\xi}}e^{(2-\sqrt{2})\pi\xi}\right)^2_{\xi=\xi_{\rm ref}}\right], & \text{for } SU(2) \end{cases} \tag{3.37}$$

where $M_{\rm Pl}$ is the reduced Planck mass, the radiation energy density today $\Omega_{R,0} = 8.4\times10^{-5}$ and the parameter ξ is proportional to the inflaton velocity

$$\xi \equiv \frac{\lambda\dot{\phi}}{2fH}\ . \tag{3.38}$$

where $\xi_{\rm cr} = \xi(x=1)$ and $\xi_{\rm ref} = \xi\left(x=(2+\sqrt{2})\xi_{\rm cr}\right)$, with $x=-k\tau$ for conformal time η. The result for the $SU(2)$ case is valid when $0.008e^{2.8\xi_{\rm cr}} \gtrsim 1/g$.

The exponential sensitivity of the gravitational wave spectrum is a key feature that allows for promising detection prospects. The GWB in eq. (3.37) is expected to be also non-Gaussian and fully chiral for large ξ [603, 614, 683], two features that can assist in the separation of sources in the GW data.

The ability of gauge fields to significantly amplify GW notwithstanding, the GW observational prospects can be limited, for Abelian models, by the risk of overproducing scalar modes [682, 684]. The non-observation of primordial black holes (PBH) places upper bounds on the scalar power spectrum. PBHs are produced when large curvature fluctuations re-enter the horizon during the radiation epoch. These PBHs must satisfy constraints on their abundance, derived from cosmological and astrophysical data [535, 685]. The statistics of the comoving curvature perturbation plays a key role in this upper bound [682, 684]: a Gaussian assumption places an approximate upper bound of $\mathcal{P}_\mathcal{R} \leq 10^{-2}$, whereas an assumed χ^2-statistics places a tighter upper bound of $\mathcal{P}_\mathcal{R} \leq 10^{-4}$.

Enforcing PBH constraints may result in a GWB sourced by axion inflation that is undetectable by ET. There are however several models that can generate a detectable GW

JCAP03(2026)081

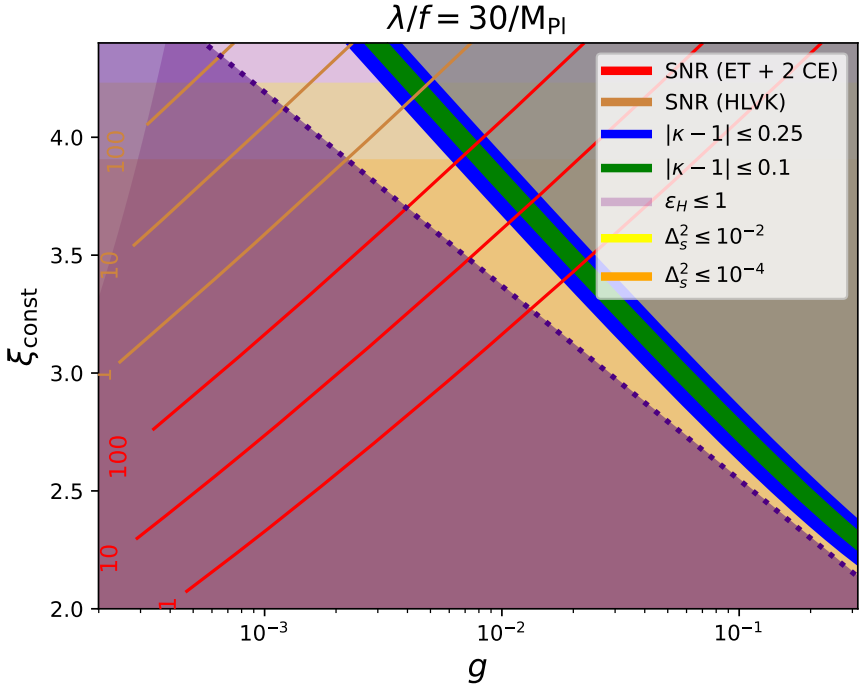

Figure 28. Backreaction and SNR prospects as a function of the gauge coupling constant g and the velocity parameter $\xi(f) = \xi_{\rm const}$ for two values of the coupling constant, $\lambda/f = 30/M_{\rm Pl}$. The Hubble rate on the CMB scale is assumed to be $H_{\rm CMB} = 2.1 \times 10^{-5}\ M_{\rm Pl}$. The brown and red lines are the SNR contours calculated assuming 1 year of observation with the design LVK and ET + 2 CE network sensitivities, respectively. The blue and green bands represent $|\kappa - 1| \leq 0.25$ and 0.1, where we expect that the PBH overproduction bound could be relaxed in the strong backreaction regime. The light purple region represents the slow-roll parameter satisfying $\epsilon_H \leq 1$, where inflation is still ongoing. Yellow and orange regions correspond to the parameter space where the primordial curvature spectrum stays below the PBH upper limit assuming Gaussian ($\mathcal{P}_\mathcal{R} \leq 10^{-2}$) and χ^2 ($\mathcal{P}_\mathcal{R} \leq 10^{-4}$) statistics. Additionally, we shade the Abelian regime in magenta (below the black dotted line) and the strong backreaction regime in gray (upper region of the $|\kappa - 1|$ band), in both of which the estimation of the SNR is not reliable. Reproduced from [689]. CC BY 4.0.

signal all the while satisfying PBH bounds. For example, $\mathcal{N} > 1$ coupled $U(1)$ gauge fields can suppress the scalar power spectrum by $1/\mathcal{N}$ in the $\xi \gg 1$ regime. Such an extension was shown to create a working linear potential for $\mathcal{N} = 6$ couplings and a working quadratic model for $\mathcal{N} = 10$ couplings [635, 684]. Recent lattice simulations of axion $U(1)$ inflation assuming a quadratic potential showed that strong backreaction close to the end of inflation can suppress non-Gaussian behavior in comoving curvature perturbation, softening the PBH bound in ground detector frequency regime [686] (see also [687] for lattice studies on Abelian models). This relaxed bound would allow this model to be detectable by GW detectors, including ET, LISA and even advanced LIGO. Extending axion inflation models with an additional pseudoscalar field different from the inflaton can provide a localised bump in the tensor and scalar spectrum. It can also create detectable GW signal that conform to PBH and CMB related bounds [684, 688], see figure 27.

JCAP03(2026)081

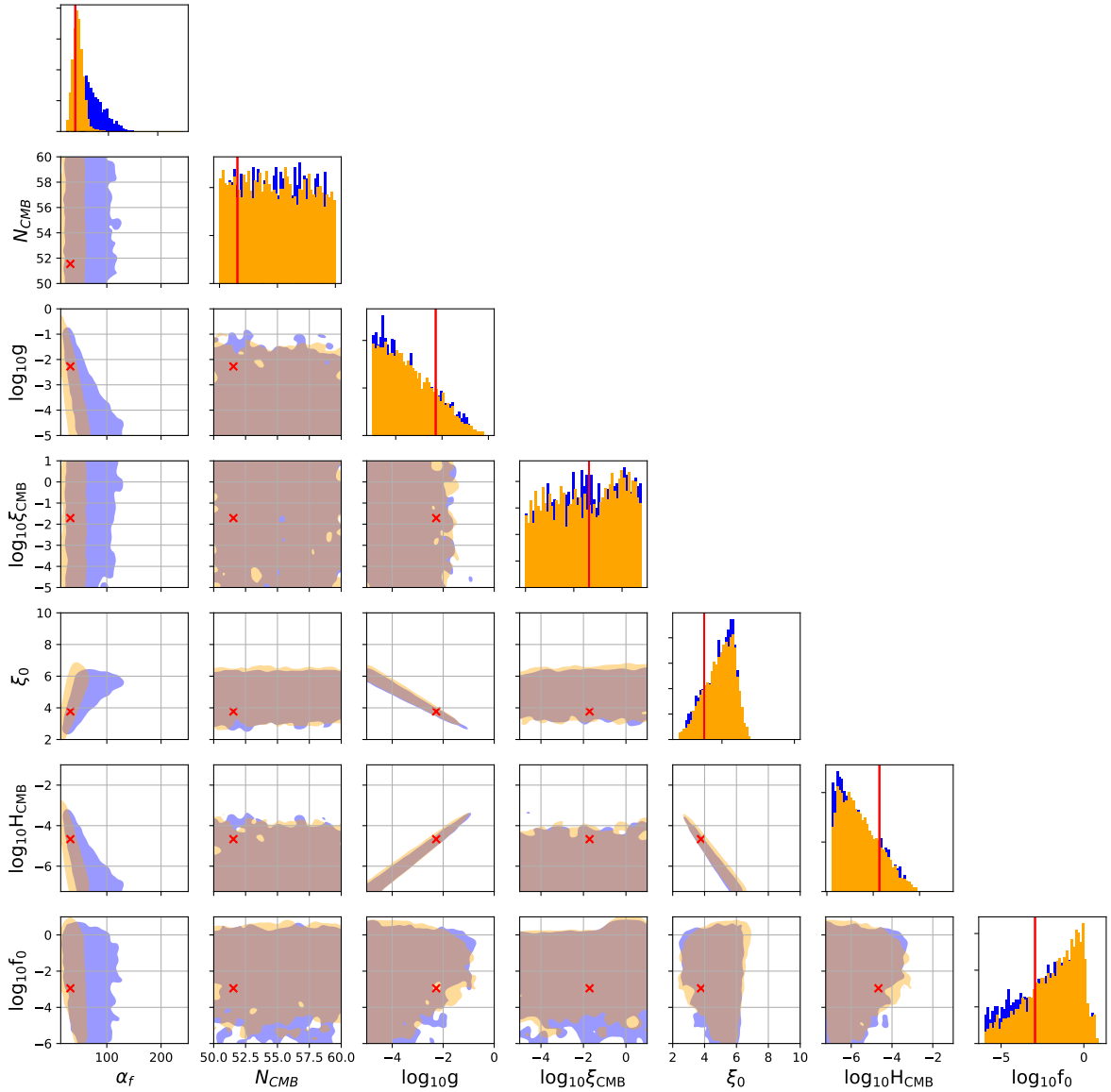

Figure 29. Posterior distributions from Bayesian inference assuming a piecewise, toy model potential, with inflaton velocity $\xi_{\rm CMB}$ before pivot frequency f_0, and velocity ξ_0 after. This search is done assuming χ^2 statistics. The shaded regions correspond to the 95% CL. The different colors used are: blue for ET and orange for a network consisting of ET+2CE. The red cross and line correspond to the injected values. Reproduced from [689]. CC BY 4.0.

The GW sourcing mechanism for non-Abelian models is rather different: GWs are sourced already at the linear level by tensor degrees of freedom in the gauge sector [605]. The sourcing mechanism for scalars being less tied to the fate of tensors amplification, PBH bounds are typically less stringent in these scenarios.

A PBH constraint in non-Abelian field contexts can limit, but does not exclude GWB detection prospects [623, 689]. A general parameter space study performed in [689] found that assuming, conservatively, a constant inflaton velocity,[17] a GWB from non-Abelian fields

[17] Inflaton velocity ξ generally increases exponentially during inflation.

JCAP03(2026)081

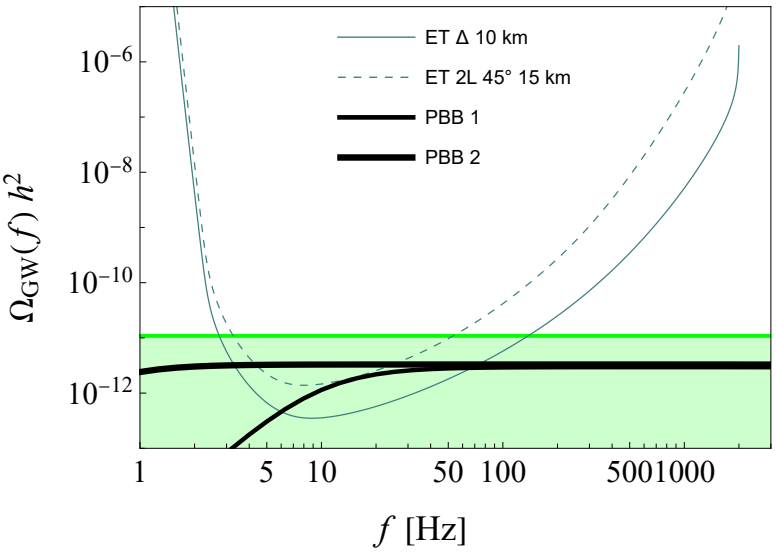

Figure 30. GWB predicted by pre-big-bang cosmology, compared with the PLS of the considered ET configurations. Here we assume an observation time of one year and SNR = 1. The shaded green area is the range of the GWB allowed by a set of consistency conditions on the parameter space of the model [690]. The GWB spectral shape is computed assuming $z_s = 5 \times 10^6$, $z_d = 10^3$, $z_\sigma = 2.2$ ("PBB 1" curve, broken power law within the ET sensitivity window) and $z_s = 10^8$, $z_d = 10^3$, $z_\sigma = 2.2$ ("PBB 2" curve, almost flat plateau within the ET sensitivity window). Here $z_s = \eta_s/\eta_1$, $z_d = \eta_d/\eta_1$ and $z_\sigma = \eta_\sigma/\eta_1$ are ratios of conformal-time scales marking four different regimes: de Sitter evolution for $-\eta_s < \eta < -\eta_1$, radiation domination for $-\eta_1 < \eta < \eta_\sigma$, matter domination for $\eta_\sigma < \eta < \eta_d$ and another radiation-domination phase for $\eta > \eta_d$.

can be 3G detectable — even with more constraining power in the χ^2-statistical assumptions, as reported in figure 28. An injection of a GWB sourced by a piece-wise scalar potential analysed using a triangular ET detector and a ET+2CE network yielded a logBayes factor for an GWB versus noise greater than 79, a confident detection. The posterior distribution of the non-Abelian and of the cosmological parameters is shown in figure 29 for different detector configurations.

3.2.1.3 Pre-big-bang cosmology. As we have seen in the previous subsection, the inflationary prediction from single-field slow-roll inflation is in general too small to be detectable by third-generation detectors. From eq. (3.35) we see that the key to having a detectable spectrum is to have $n_T > 0$ (i.e., a "blue" spectrum), at least up to the ET frequencies. Eventually, the slope will have to flatten until it reaches a cutoff, in order not to violate upper bounds on $h_0^2\Omega_{gw}(f)$, such as the Big-Bang Nucleosynthesis (BBN) bound, that requires that the integral of $h_0^2\Omega_{gw}(f)$ over $d\log f$ will be smaller than $\mathcal{O}(10^{-6})$ [691].

A model that displays such a behavior is the so-called "pre-big-bang" cosmology [692, 693], which emerges quite naturally from the low-energy effective action of string theory, and predicts a blue tensor spectrum [694, 695]. The GWB of this model roughly has a bell-shaped form characterized by a maximal flat plateau whose length in frequency can vary from zero (maximum peak) to a wide interval, depending on the value of the theoretical parameters [690].

JCAP03(2026)081

The portion of this shape falling into the ET frequency range is either a flat signal (the plateau at maximal amplitude) or a broken power law; see figure 30. In the latter case, the GWB raises as f^3 at low frequencies and then, at some frequency f_s, it changes slope to f^0; f_s must be taken as a free parameter, since it depends on the details of the cosmological evolution in the high-curvature phase of the model [696, 697]. The spectrum then drops down at higher frequencies not shown in the plot.

3.2.2 GWs from phase transitions

One of the possibly strongest sources of GWs from the early Universe is a cosmological first-order phase transition [624] that could lead to large observable signals at next-generation GW observatories. The peak frequency of the signal is fixed by the temperature of the Universe at the time of the phase transition. Particularly interesting is the case of the electroweak phase transition that would give rise, if it is first-order, to a GW signal in the milliHertz range observable at LISA [537, 698–702]. ET would be a window on phase transitions happening much earlier, and would therefore probe particle physics that is well beyond the reach of particle colliders.

While the Standard Model of high energy physics does not exhibit any first order phase transitions, numerous Beyond Standard Model (BSM) scenarios do. Quantum field theory and string theory typically feature a complicated vacuum manifold with several coexisting minima. The unknown evolution of the early Universe might have populated, possibly via the mechanism of symmetry restoration, false vacua and lead to a series of phase transitions (PTs) between the minima of the manifold. The larger the latent heat released during the transition, the stronger is the resulting GW signal. In this context, first-order PTs (FOPTs) proceed via the stochastic nucleation of spherical bubbles of the new phase in the old phase, with the probability of nucleation per unit of time and volume controlled by stochastic processes

$$\mathcal{P}_{\text{nucleation}} \propto A(t) e^{-\mathcal{S}_c(t)}\,, \tag{3.39}$$

where $\mathcal{S}_c(t)$ is the euclidean action of the critical bubble. The bubbles subsequently grow and fill the space until the total conversion of the plasma to the true minimum. In this process they produce GWs that can be observed at ET. There are two crucial steps on mapping the BSM physics parameters (couplings, mass scales) to the induced GW signal. The first step consists in mapping the BSM parameters to the thermal description in terms of energy budget parameters. The energy released during the PT can be quantified by the ratio between the energy stored in the vacuum and in the plasma at the moment of the transition [700, 701, 703]

$$\alpha(T) \equiv \frac{\Delta V(T) - T\frac{\partial \Delta V}{\partial T}}{\rho_{\text{rad}}} \qquad \text{(Strength parameter)}, \tag{3.40}$$

which has to be evaluated at the percolation temperature. A second important parameter is the duration of the phase transition. The duration from the nucleation to the percolation can be approximated by expanding the rate of nucleation at first order and leads to the definition

$$\tilde{\beta} \equiv \frac{\beta}{H} = -\frac{d(\mathcal{S}_c/T)}{H dt} \qquad \text{(Duration of the transition)}\,. \tag{3.41}$$

JCAP03(2026)081

The normalised speed of nucleation $\tilde{\beta} \propto t_{\rm expansion}/t_{\rm transition}$, with $t_{\rm transition}$ the typical time the transition takes to complete and $t_{\rm expansion}$ the Hubble time, measures how fast a bubble nucleates with respect to the expansion of the Universe, giving an estimate of the speed of completion of the transition. This value can be related to the size of the bubbles at collision via [701, 704, 705]

$$R_{\rm coll} = \frac{(8\pi)^{1/3}}{H_{\rm reh}\beta}\,. \tag{3.42}$$

Note that in the case in which the phase transition is seeded by topological defects [625, 706, 707], the duration of the transition and the bubble size are instead related to the number of defects per Hubble volume, affecting also the GW signal [708–712].

Assuming that the transition occurs in less than an Hubble time, we can apply conservation of energy arguments to obtain the *reheating temperature* $T_{\rm reh}$:

$$(1-\Omega_{\rm GW})(\Delta V + \rho_{\rm rad}|_{T=T_{\rm per}}) = \rho_{\rm rad}|_{T=T_{\rm reh}} \qquad \Rightarrow T_{\rm reh} \approx (1+\alpha)^{1/4} T_{\rm nuc}\,, \tag{3.43}$$

where we neglected the energy lost in the GW signal.

The terminal velocity of the bubble wall v_w of the bubble has been the subject of intense investigation, as it requires to solve a very non-trivial set of coupled equations. Estimates of the terminal wall velocity are usually based on kinetic theory [713–716], improvement of it [717–719], or holographic methods for strongly coupled theories [720–724] (see ref. [725] for a quasiparticle (quasigluons) method). Typically, calculating the terminal wall velocity is a very challenging task, and has only been performed for a limited number of models [714–716, 719, 726, 727]. In such computations, one needs to solve the scalar field equation of motion (EoM) coupled to the Boltzmann equations describing the particles in the plasma. Simplifications can be obtained by assuming local thermal equilibrium (LTE) [728–735] or in the ultrarelativistic regime [736–742]. Schematically, this mapping can be written

$$\boxed{\text{BSM parameters}(\texttt{couplings}, \texttt{masses}\ldots) \Rightarrow (\alpha, \beta, T_{\rm reh}, v_w)\,.} \tag{3.44}$$

The second matching consists of the prediction of the features of the GW signal, namely, the shape of GW spectrum, the peak amplitude $\Omega_{\rm GW,peak}$, and the peak frequency $f_{\rm peak}$, from a set of $(\alpha, \beta, T_{\rm reh}, v_w)$. Schematically

$$\boxed{(\alpha, \beta, T_{\rm reh}, v_w) \Rightarrow (f_{\rm peak}, \Omega_{\rm peak}, \text{GW spectrum})\,.} \tag{3.45}$$

The spectrum of the GW signal depends strongly on the source and requires to be simulated. The process of expansion and collision of those bubbles of true phase will generate GWs via three distinct mechanisms: i) from the *bubble collision*, where the energy collected in the scalar shell on the bubble wall is released at collision [743–748], ii) from the *sound waves* where the energy injected in the plasma propagates under the form of sound waves [705, 749–751, 753–755], iii) from the *turbulence* occurring when the sound waves decay [756] (see also [752] for another source of GWs). It is typically found to be well fitted by a *broken power-law* of the type

$$\Omega_{\rm GW}(f) \propto \frac{(a+b)^c f_{\rm peak}^b f^a}{(b f_{\rm peak}^{\frac{a+b}{c}} + a f^{\frac{a+b}{c}})^c}\,, \tag{3.46}$$

JCAP03(2026)081

Reference and group	IR tail	UV tail
Envelope simulation [743] Ω_ϕ	3	1
Envelope simulation [744] Ω_ϕ	$2.9^r - 2.95$	$0.9 - 1$
Envelope analytic [745, 746] Ω_ϕ	3	1
Bulk flow [744] Ω_ϕ	$0.95 - 0.9^r$	$2.9 - 2.1^r$
Lattice Simulation [747] Ω_ϕ	3	~ 1.5
Lattice Simulation [748] Ω_ϕ	$0.68 - 1.56$	$1.35 - 2.25$
Sound Shell model [749, 750] Ω_{sw}	9	4
Analytic [746] Ω_{sw}	3	1
Hybrid simulation [751] Ω_{sw}	3	3
Lattice Simulation [705] Ω_{sw}	3	4
Analytic and simulations [752] $\Omega_{\rm FS}$	1	2

Table 3. Shape of the GW signals from some of the different groups working on GW from FOPT in the UV and the IR. Results are shown under the form of $(f/f_{p,0})^n$ for the IR and $(f/f_{p,0})^{-n}$ for the UV tail. The suffix r means that the result is specific to relativistic walls. The mismatch between numerical simulations and the current models available (Sound shell and Bulk flow) motivates us to investigate further the analytic understanding of GW from bubble collision.

with parameters a, b, c given by simulations. In table 3 we report the slope in the UV and in the IR for different simulations for the Ω_ϕ (bubble collision source), the Ω_{sw} sound wave sources and from the free-streaming source $\Omega_{\rm FS}$. Even if it seems that the spectra from the sound waves and the bubble collisions are very different for small α, it was recently argued that the spectra from the sound-waves in the regime of large α resembles the spectrum of the bubble collision [757].

The typical frequency peak $f_{\rm peak}$ is controlled by the temperature $T_{\rm reh}$ after the completion of the PT and the size of bubbles at collision $R_{\rm coll}$:

$$f_{\rm peak} \approx \mathcal{O}(1) \times 10^{-5} \frac{1}{H_{\rm reh} R_{\rm coll}} \frac{T_{\rm reh}}{100\,{\rm GeV}}\ {\rm Hz}\,, \tag{3.47}$$

where $H_{\rm reh}$ is the Hubble constant after the completion of the PT and a $\mathcal{O}(1)$ factor depending on the details of the source. Figure 31 shows the expected spectra from sound waves, while figure 32 shows the parameter spaces of FOPT that can be probed by ET.

Testing particles physics model would consist in inverting the steps that we have made so far. Assuming an observed stochastic signal, we have to perform the inverse problem

$$\boxed{({\rm GW\ spectrum}, f_{\rm peak}, \Omega_{\rm GW,peak}) \Rightarrow (\alpha, \beta, T_{\rm reh}, v_w) \Rightarrow {\rm BSM\ parameters}\,.} \tag{3.48}$$

Supercooled phase transitions in particular lead to very strong signals (large α, small β/H). This arises in particular naturally in models featuring nearly-conformal dynamics [760–762]. Such supercooled PTs and their associated signals were studied extensively in the context of new TeV physics [763–765] but the same physics can be readily applied to strong dynamics occurring at higher energies that could be connected to dark matter and that would lead to signals in the ET window [766].

JCAP03(2026)081

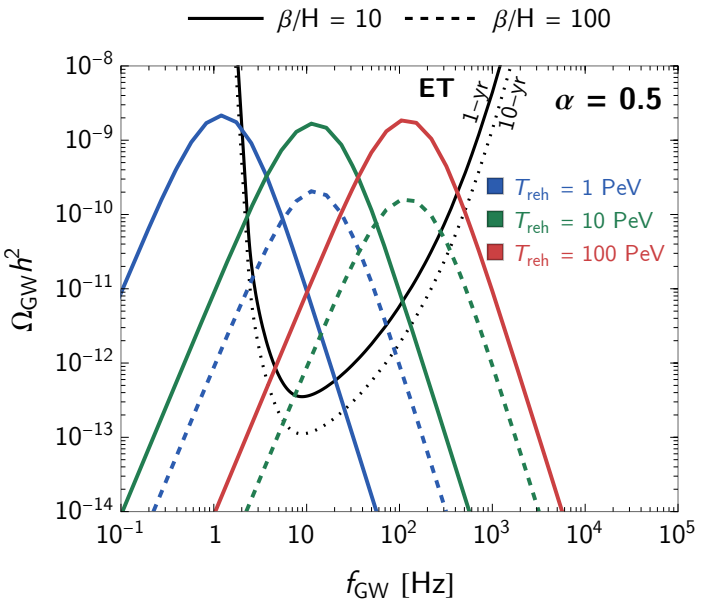

Figure 31. GW spectra from sound waves produced by first-order FOPTs at temperature $T_{\rm reh}$ [701], with the wall velocity that gives the maximal energy transfer to sound waves [758, 759]. The black curves are the power-law integrated sensitivities of ET assuming a triangular xylophone configuration with 10km arms and the 1 and 10 years observation time with SNR = 1.

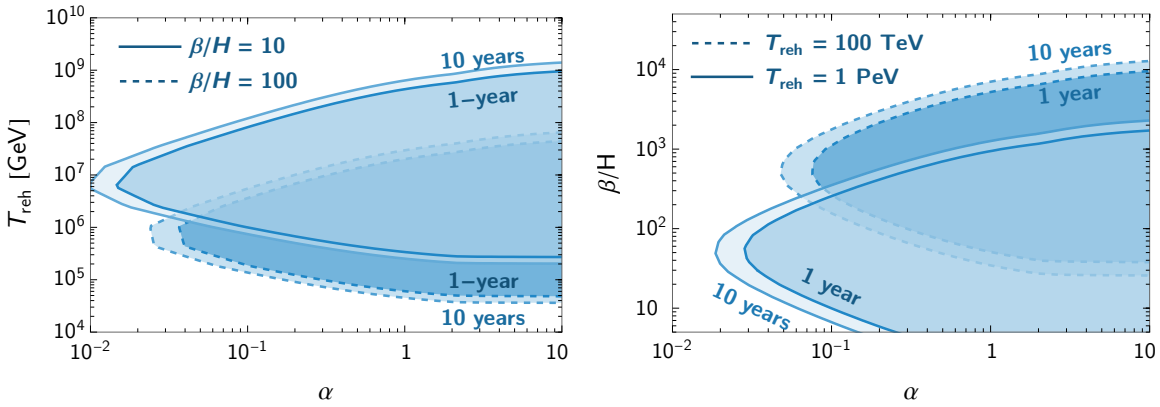

Figure 32. Regions of FOPT parameter spaces that can be probed by ET assuming triangular xylophone configuration with 10km arms for two values of β/H (left) and $T_{\rm reh}$ (right), assuming GW from sound waves [701] shown in figure 31. The darker regions can be probed with ET at SNR ≥ 1 and 1 year of observation time, while the lighter regions require 10 years.

JCAP03(2026)081

Going back to eq. (3.47), as can be seen from figure 31, this GW signal would roughly lie in the detection range of the ET detector, f between a few Hz and a few 10^3 Hz, if the ratio $(H_{\rm reh}R_{\rm coll})^{-1}(T_{\rm reh}/100{\rm GeV})$ is between a few times 10^5 and a few times 10^8, i.e. for PTs largely above the EW scale. In this detection range, the LVK collaboration could also constrain large regions of parameter space, specially in the case of models featuring large supercooling, such as the conformal models [767–769], Pati-Salam models [770], high energy $B-L$ breaking PT [771], SUSY breaking [772, 773], Peccei-Quinn symmetry breaking [774, 775], flavour models [776, 777], models with extended gauge groups [778–781], and the remnant of the confinement of a hypothetical composite Higgs [765, 782–784] (see also [785–787] for more general studies). Other physical phenomena related to signals in ET have also been envisioned, such as bubble wall enhanced phenomenon like baryogenesis [788–790], leptogenesis [791, 792], Dark Matter production [766, 779, 793–795], and could be in the reach of detection of ET. This exciting possibility motivates us to strengthen the relation between model building parameters and observables in ET telescope.

3.2.3 GWs from cosmic strings

3.2.3.1 Local and global strings. Topological defects of various kinds — including cosmic strings and domain walls (see section 3.2.4) — may form in symmetry-breaking phase transitions in the early Universe [796]. In particular, if the vacuum manifold contains non-contractible loops then a network of strings can be produced, and (if they are dynamically or energetically stable) they will still be present in the Universe until today. Cosmic strings are referred to as *local/global* depending on the nature of the underlying symmetry groups (see [797–800] for reviews on cosmic strings). Local cosmic strings are ubiquitous in supersymmetric grand unified theories: indeed all models which solve the monopole problem, lead to baryogenesis after inflation and are consistent with proton lifetime measurements form local strings [801]. Global strings on the other hand are characteristic of axion models, and are formed for instance when the Peccei-Quinn symmetry is broken after inflation [802–804]. The global strings in these models can become unstable at a later stage when a subsequent symmetry breaking phase transition leads to the formation of domain walls [802–807] (see also section 3.2.4).

Both local and global string networks (and indeed domain-wall networks) can source gravitational waves (GWs), and this production occurs throughout the lifetime of the network, from the initial phase transition to the present day. As a result, strings produce a GWB spectrum which generally covers a very broad range of frequencies (see e.g. [808]), and hence can be probed by experiments in different frequency bands — from the nHz and pulsar timing array (PTA) experiments [421, 809, 810], to the mHz and LISA [808], up to the 1–10^4 Hz band of ET and other ground-based interferometers. Furthermore, if a string is sufficiently close to us, the characteristic bursts of GWs it emits [811, 812] can be searched for individually [129]. Both type of observations (bursts or GWB) can put constraints on the energy scale of the phase transition in which strings are formed, η, and can thus reveal the properties of the phase transition and particle physics at that energy scale.

JCAP03(2026)081

Local strings have a characteristic width $w \sim 1/\eta$ and finite energy per unit length which (in units $\hbar = c = 1$), is given by

$$G\mu \sim 10^{-6} \left(\frac{\eta}{10^{16}\ \text{GeV}} \right)^2 . \tag{3.49}$$

Local strings predominantly lose energy into GWs. In contrast, global strings dominantly radiate Nambu-Goldstone bosons, and the existence of this Nambu-Goldstone radiation leads to a time-dependent, logarithmically-divergent energy per unit length

$$G\mu(t) \sim 10^{-6} \left(\frac{\eta}{10^{16}\ \text{GeV}} \right)^2 \log \left(\frac{H^{-1}(t)}{w} \right) , \tag{3.50}$$

where $H(t)$ is the Hubble parameter.

In the remainder of this section, focusing on the ET frequency band, we summarise the burst and GWB signatures of both local and global strings, taking into account existing observational constraints. Beyond the minimal cosmic-string models — depending only on $G\mu$ (or equivalently η) — discussed here, there are several other well-motivated cosmic-string models that depend on additional parameters, modifying the string-network dynamics and leading to interesting features on GWB. These include the superstrings [813–818], the metastable cosmic strings [797, 819–829], Hubble-induced strings [830] and superconducting strings [831–834]. Although their GWB and features are relevant for ET, these models are subjected to some uncertainties and will need more numerical studies in order to draw robust predictions.

3.2.3.2 Gravitational waves from local strings. Due to the vast separation of scales between the length and the width of a cosmic string, it is often convenient to describe their dynamics in the zero-width limit. For local strings, this results in a Nambu-Goto action characterised purely in terms of $G\mu$. Cosmic string networks can also be studied using lattice field theory simulations (see, e.g., [835–837]). The results from these simulations have sparked a long-standing debate on how to reconcile these two types of simulations. Recent studies however suggest that indeed field theory string loops coming from cosmic string network simulations evolve as Nambu-Goto dictates [838]. On the other hand, it is clear that more work in this direction is needed to conclusively show the agreement between these two approaches. Here we will concentrate of the predictions from Nambu-Goto strings.

This Nambu-Goto approximation has been used extensively in the literature to investigate the dynamics of local string networks (see, e.g., refs. [797, 798, 808, 839] for reviews). The picture that emerges is that each Hubble patch contains $\mathcal{O}(1)$ 'long' superhorizon strings, which continually produce closed string loops by self-intersecting. These loops evolve periodically over time, expanding and contracting at relativistic velocities due to their tension. This relativistic dynamics results in strong GW production from loops, particularly via pronounced features such as cusps (string segments which move instantaneously at the speed of light), kinks (discontinuities in the tangent vector along the loop), and kink-kink collisions [811, 840, 841]. As a result, loops decay in size and energy via GWs long kinky strings [842] at a rate $\mathrm{d}E/\mathrm{d}t \approx -\Gamma_{\rm GW} G\mu^2$ (with $\Gamma_{\rm GW} \approx 50$ a dimensionless coefficient [841, 843, 844]), radiating at increasingly high frequencies until they vanish from the network. This decay of individual

JCAP03(2026)081

loops, combined with the continuous production of new loops from the self-intersection of 'long' strings, leads to an attractor solution in which the distribution of loop sizes and the total energy contained in the network scale with the expansion of the Universe [845]. This is the so-called *scaling solution*. Evidence of this attractor solution has been found in many of the numerical simulations of string networks (see, e.g., [839, 846–848]).

Early attempts to detect local strings focused mostly on their imprints on the cosmic microwave background (CMB) due to the deflection of CMB photons, resulting in constraints of $G\mu \lesssim 10^{-7}$ [849–852]. However, the advent of GW astronomy has enabled much more sensitive searches, and therefore much more stringent constraints on the string tension, as we discuss below. The main theoretical uncertainty in these searches is the loop size distribution reached by the network in the scaling regime. The two most well-established models for this distribution — which we refer to here as model A [853] and model B [854] (based on [855]) — predict different abundances of small loops, and therefore different GW signatures, particularly at the higher frequencies relevant to ground-based interferometers such as ET and LIGO/Virgo/KAGRA. For a discussion of the origin of this discrepancy on the loop number density of non-self-intersecting loops computed from different simulations see [856, 857].

Another important theoretical uncertainty on the computation of the GW signatures of cosmic strings comes from the role played by gravitational back-reaction on the loop's evolution. The emission of gravitational radiation from loops modifies their shape altering their power spectrum. This effect has been recently studied analytically as well as numerically from a small number of loops [858–862]. However, its impact on the final gravitational wave signals coming from strings has only been discussed on simple toy model description in [844].

3.2.3.3 GWs from global strings. The dynamics of global strings can be described effectively as Nambu-Goto strings coupled to the Goldstone-boson field using the Kalb-Ramond action [863–865]. This additional coupling affects GW production in two ways. First, the evolution of the global-string network is modified by the back-reaction from Goldstone emission [866–868] in competition with the loop-chopping; this affects the loop number density. Second, a global-string loop only lives for a short time after its production because it decays quickly into Goldstone bosons at the rate $\mathrm{d}E/\mathrm{d}t \approx -\Gamma_{\rm gold}\mu/\log(H^{-1}/w)$ with $\Gamma_{\rm gold} \approx 65$ [864], which is $\mathcal{O}(1/(G\mu))$ more efficient than GW emission. Similarly to local strings, long global strings emit Goldstone bosons [869]. As a result, the GW production from loops is roughly the same as the time of loop production, and is therefore diluted more by Hubble expansion than in the local-string case. The resulting GWs are highly suppressed compared to those from local networks formed at the same symmetry-breaking scale [870–873]. In the case of axion strings, the spectrum is cut off at frequencies below a threshold set by the axion mass due to the strings decaying. However, for axion mass below $10^{-22}\,\mathrm{eV}$ and axion decay constant $\sim 10^{15}\,\mathrm{GeV}$ that do not cause dark matter overproduction [805–807, 873–878], this cutoff is well below the ET frequency band, so can be neglected here. (This cutoff is relevant however for low-frequency GW observations, e.g. with PTAs [873, 879].)

GW predictions for global strings must be treated with care, as there are several unresolved theoretical uncertainties. Many lattice simulations have attempted to verify whether the global string network actually reaches the scaling regime or has its string correlation length

JCAP03(2026)081

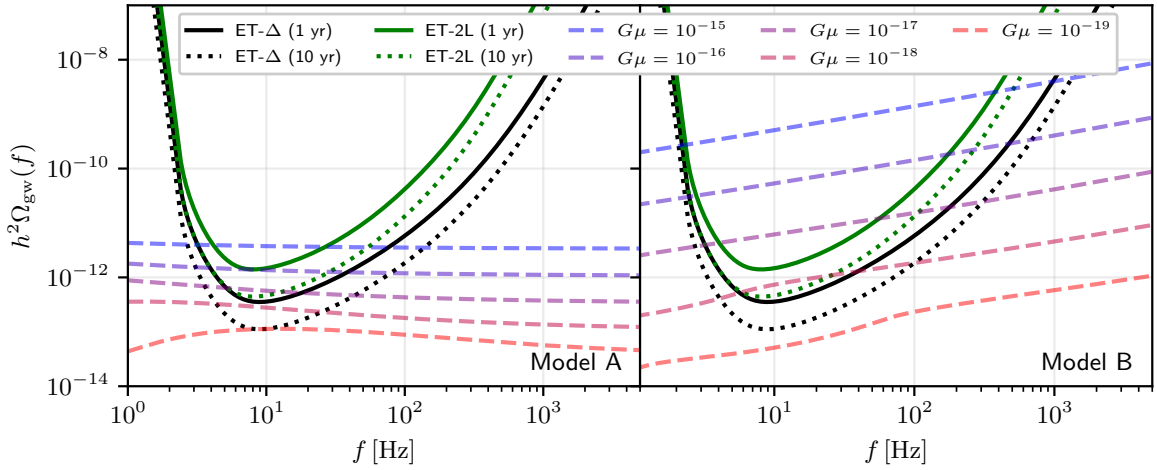

Figure 33. Forecast power-law-integrated GWB sensitivity of ET, compared with signals from local Nambu-Goto strings of various tensions $G\mu$. We consider both the triangular configuration for ET with 10 km arms, and the 2L configuration with 15 km arms, misaligned as in [16]; the solid black curves corresponds to one year of observations, while the dotted black curve corresponds to 10 years. The left and right panels show the predictions for models A [853] and B [854] of the loop network, respectively. Both models predict that, in the triangle configuration, ET will be sensitive to $G\mu \gtrsim 10^{-18}$ after one year of observations with SNR ≥ 1.

corrected with $\log(H^{-1}/w)$ [866, 868, 873, 875–878, 880–884]. Moreover, the recent debate on the powers of emissions into GW, Goldstone bosons, and massive radiation in different numerical simulations is open [873, 885–888], e.g., the amplitude of the GW signal can be smaller by $\log^2(H^{-1}/w)$ than the previous expectation [888].

In addition to GWs, the massless Goldstone production from global strings is subject to strong constraints on the number of relativistic degrees of freedom present at BBN and CMB scales, $N_{\rm eff}$. Accounting for uncertainties in the global-string network evolution, this constraint bounds the energy scale of the string network formation to be $\eta \lesssim (1-3) \times 10^{15}\,$GeV [872, 873]. The bound from deflection of CMB photons ($G\mu(t_{\rm CMB}) \lesssim 10^{-7}$) also gives similar constraints [870–873].

3.2.3.4 GW background from strings. The incoherent superposition of GWs from many string loops gives rise to a GWB signal, whose amplitude and spectral shape are determined by the symmetry-breaking scale η (which in the case of local strings corresponds one-to-one with the string tension $G\mu$), as well as by the loop network modelling as discussed above. As mentioned above, the signal spans many decades in frequency, due to the very broad range of loop sizes and emission epochs involved in the network. As a result, it is possible to set complementary constraints on string scenarios with multi-band GW observations. For local strings, results from the LVK O3 stochastic search rule out $G\mu \gtrsim 10^{-8}$ for model A and $G\mu \gtrsim 4 \times 10^{-15}$ for model B [129], while the most recent results from NANOGrav and EPTA each rule out $G\mu \gtrsim 10^{-10}$ for both models A and B [421, 809, 810]. (This assumes that the GWB signal detected by these PTAs is due to inspiralling supermassive

JCAP03(2026)081

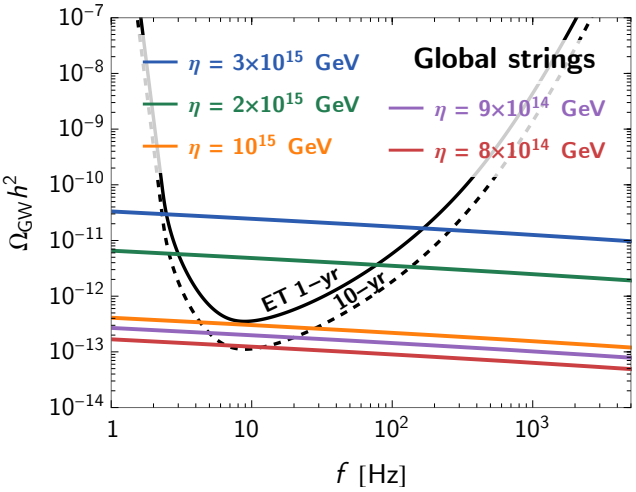

Figure 34. Spectra of GWB from global strings formed at energy scale η are shown in solid colored lines. The black lines are the same ET-triangle sensitivity curves as shown in figure 33. We used the semi-analytic calculation in [871]; see also [870, 872].

binary black holes [889]; several more exotic explanations for this signal have been proposed, including cosmic strings.)

These constraints will improve drastically with next-generation GW observations in the 2030s. The space-based interferometer mission LISA, which has recently undergone ESA adoption [330], is expected to be sensitive to local string networks with $G\mu \gtrsim 10^{-17}$ (for both models A and B) [808]. As shown in figure 33, we can expect even stronger constraints from ET. In the triangular 10km configuration we can probe string tensions $G\mu \gtrsim 10^{-18}$ with just one year of data both for models A and B, while with the 2L 15km aligned configuration we can probe $G\mu \gtrsim 10^{-19}$, for model A, and slightly smaller for model B [16].

For global strings, as shown figure 34, we can expect ET to probe $\eta \gtrsim 8 \times 10^{14}\,\mathrm{GeV}$. This sensitivity is comparable to that of LISA [871–873], while for the most recent PTA data from e.g., NANOGrav, one obtains $\eta \gtrsim 3 \times 10^{15}\,\mathrm{GeV}$ [879], which is comparable to the current constraints from Nambu-Goldstone radiation. ET will therefore improve upon these current constraints; however, these other constraints are also likely to improve by the time ET is operational, e.g., due to stage-4 CMB surveys [890].

3.2.3.5 GW bursts from strings. Strong bursts from nearby cosmic string loops may be resolved in GW detectors and searches are currently undertaken with the hope to detect individual cusps or kinks in LVK datatsets [129, 891] as well as PTA data [892]. Similar searches will also be carried out in the future for LISA [330, 893, 894]. Here we forecast the capabilities of ET to detect individual cusps assuming a single detector with a triangular xylophone configuration with 10km arms (ET LF+HF) [16].

As a first approximation, we compute the combined SNR of individual bursts using the response function for a triangular detector [529] and claim a detection if the SNR is above 20. Accurate data analysis would rely on match-filtering methods or new methods such as machine learning [895]. Similarly to the procedure already described for LISA [894],

JCAP03(2026)081

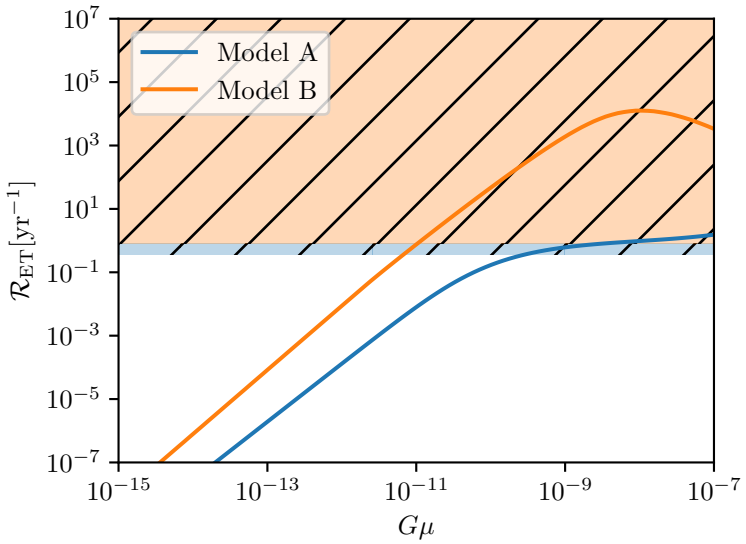

Figure 35. Expected rate of detected bursts in Einstein Telescope as a function of the string tension for models A and B. In case ET does not detect bursts from cosmic string cusps, the orange hatched region is excluded after 4 years of observations and the blue hatched region is excluded after 8 years.

we simulate a set of sources with random polarization and sky-localization, and obtain the average response function of ET to cosmic string bursts as a function of their amplitude. We then combine the response function of ET with the rate of bursts predicted for different loop population models to obtain the expected rate of bursts detected in ET.

The expected burst rates for both models A and B are presented in figure 35. For $G\mu \approx 10^{-11}$ compatible with the PTA signal [421, 809, 810], one expects to detect about one burst per year for B and 10^{-2} for A. If ET does not detect bursts from cosmic string cusps, it would place constraints on the abundance of loops in our cosmic neighbourhood, and constrain the string tension to $G\mu \lesssim 10^{-11}$ for B and $G\mu \lesssim 10^{-10}$ for A.

Note however that the computation of these rates have not taken into account the effect of gravitational back-reaction. This could not only affect the typical number of cusps per loop but also their persistence in time.

3.2.4 GWs from domain walls

Domain walls (DWs) are two-dimensional defects (surfaces) that separate regions of space belonging to physically different vacua of the theory. These vacua are typically related by a global discrete symmetry, so that they are exactly degenerate in energy and the DWs are topologically stable. As the DW configuration interpolates between discrete minima, the corresponding field is forced to leave the vacuum manifold at the center of the wall, so that its energy density can in fact be very high. Domain walls can possibly lead to a cosmological problem if they are absolutely stable and eventually dominate the energy density of the Universe. Solutions to this problem come with interesting phenomenological consequences for the domain wall network, as we will discuss.

JCAP03(2026)081

Domain walls arise in many beyond Standard Model theories where the symmetry of the SM is extended and a discrete group (or subgroup) of this symmetry is spontaneously broken during the cooling of the Universe. The list of motivated models is large and includes: discrete flavor symmetries [896, 897], two-Higgs [898, 899], twin-Higgs [900, 901], composite Higgs [902, 903] models, non-Abelian flavor symmetries [896, 897], axion monodromy [904, 905], supersymmetry [906–910], grand unification [911–913], Hubble-induced phase transitions [914, 915] and discrete spacetime symmetries [916–921].

QCD axion models [435–438] are of particular interest. While solving the strong CP problem of the Standard Model, they lead naturally to DWs [802, 803, 922]. The underlying Peccei-Quinn (PQ) mechanism introduces a new global $U(1)_{\rm PQ}$ symmetry that is spontaneously broken at a high scale F_a and it is anomalous under QCD [435, 436]. At low energies, the model consists of the (pseudo-)Goldstone boson, the axion, coupled to topological defects: global strings, and DWs. See also [923–927] and [439, 441, 928–939] for recent reviews on several aspects related to axion models and phenomenology.

In post-inflationary scenarios, the cosmological PQ phase transition leads to the formation of a network of $U(1)_{\rm PQ}$ global strings. At much lower temperature, $T \sim \Lambda_{QCD}$, QCD further breaks $U(1)_{\rm PQ}$ to a discrete subgroup $Z_{N_{\rm DW}}$, and DWs appear. The integer $N_{\rm DW}$ is the number of DWs attached to each string and is a model dependent parameter (it relates to the PQ charges of SM and/or heavy quarks). If $N_{\rm DW} = 1$, the string network is quickly annihilated at $T \sim \Lambda_{QCD}$ and negligible GWs are produced. Instead, if $N_{\rm DW} > 1$ a string-wall network is formed and some additional $U(1)_{\rm PQ}$ breaking sector enforces DW annihilation.

As a result, QCD axion models with $N_{\rm DW} > 1$ naturally lead to a DW epoch and so to potentially a sizeable GW signal. Numerical simulations in this scenario were performed in [940]. The signal is strongest in heavy QCD axion, which are themselves of particular interest because they address the axion 'quality' problem [941–960], see also [961–966]. Importantly, in these models the amplitude of GW observables is correlated with the proton and neutron electric dipole moments [961, 962], which is a welcome feature towards possible degeneracies in interpretations.

The relevance of DWs in cosmology has been pointed out a long time ago [796, 967]. The typical setup involves the spontaneous breakdown of a discrete symmetry during the thermal history of the Universe. Regions of space separated by distances that are larger than the correlation length of the field around the temperature of the phase transition will randomly select one among the possible vacua of the theory. DWs will then form at the boundaries between these causally-disconnected regions where the field remains trapped at the maximum of the potential.

The resulting DW network is characterized by the tension σ, which measures the DW energy (or mass) per unit surface, and the correlation length, R, indicating the typical distance between the walls as well as their average curvature radius. The evolution of the network in a cosmological setting is determined by the tendency of the walls to reduce their energy by reducing their surface, as well as by the Hubble expansion and the effect of friction with the surrounding plasma. When particle friction can be neglected, the network is known to approach an attractor solution independently of the initial conditions in which the correlation length is set by the Hubble horizon, $R = \xi H^{-1}$, with constant $\xi = \mathcal{O}(1)$

JCAP03(2026)081

indicating the average number of DWs per Hubble patch. In this so-called scaling regime, the energy density of the network is

$$\rho_{\rm DW} = 2\mathcal{A}\,\sigma H, \tag{3.51}$$

with $\mathcal{A} = \mathcal{O}(1)$. It appears from the scaling in (3.51) that the DW energy density will eventually take over the energy in matter and radiation leading to an inconsistent cosmology [803, 967, 968]. This conclusion can be avoided if the DWs still remain a subdominant component of the energy budget today. This can occur if the DW tension is small enough, or in case a period of inflation has provided sufficient dilution of the network. These two options inevitably suppress most of the signals coming from the DWs.[18] We will instead consider a third possibility in which the DW network is actually metastable and it undergoes annihilation at a temperature $T_{\rm ann}$ when its energy density is still far from domination.

As mentioned before, DWs related to exact discrete symmetries are topologically stable and cannot annihilate. To allow for annihilation one then needs to introduce an explicit breaking of the underlying discrete symmetry so that the degeneracy of the vacua is lifted by a small bias ΔV. This introduces an additional force acting on the network, namely a vacuum pressure towards the true vacuum of the theory. At the early stage of the evolution, the bias has no effect and the network can still reach the scaling regime. However, at the temperature $T_{\rm ann}$ when the vacuum pressure balances the tension force σ/R, the friction with the plasma as well as the Hubble expansion, the network begins to collapse. One estimates this temperature to be related to ΔV as [940, 972–974]

$$T_{\rm ann} \simeq 270\ {\rm MeV} \left(\frac{\sigma^{1/3}}{100\ {\rm TeV}}\right)^{-3/2} \left(\frac{\Delta V^{1/4}}{100\ {\rm MeV}}\right)^{2} \left(\frac{g_*}{10}\right)^{-1/4}. \tag{3.52}$$

Annihilation at $T_{\rm ann}$ results in the copious production of gravitational waves, particle excitations and (as discussed in section 3.2.5.3) possibly additional relics such as primordial black holes. The energy budget available from the DW annihilation can be parameterized by $\alpha_{\rm ann}$ given by

$$\alpha_{\rm ann} \equiv \frac{\rho_{\rm DW}}{\rho_{\rm tot}}\Big|_{\rm ann} \simeq 0.02 \left(\frac{\sigma^{1/3}}{100\ {\rm TeV}}\right)^{3} \left(\frac{T_{\rm ann}}{100\ {\rm MeV}}\right)^{-2} \left(\frac{g_*}{10}\right)^{-1/2}, \tag{3.53}$$

with $\rho_{\rm tot} = 3H^2 M_{\rm Pl}^2$ the total energy density, and $\alpha_{\rm ann} < 1$ to avoid DW domination. The corresponding spectrum of GWs is characterized by a peak amplitude

$$\Omega_{\rm peak} \simeq 1.64 \times 10^{-6} \left(\frac{\tilde{\epsilon}_{\rm gw}}{0.7}\right) \left(\frac{\mathcal{A}}{0.8}\right)^{2} \left(\frac{g_*(T)}{10}\right) \left(\frac{g_{*s}(T)}{10}\right)^{-4/3} \alpha_{\rm ann}^2\,, \tag{3.54}$$

with $\tilde{\epsilon}_{\rm gw}$ an $O(1)$ efficiency factor, and the peak frequency is

$$f_{\rm peak} \simeq 1.15 \times 10^{-9}\ {\rm Hz} \left(\frac{g_*(T)}{10}\right)^{1/2} \left(\frac{g_{*s}(T)}{10}\right)^{-1/3} \left(\frac{T_{\rm ann}}{10\ {\rm MeV}}\right). \tag{3.55}$$

[18] Another possibility is that the domain wall tension decreases with time, eventually leading to the melting of the DW network [969–971].

JCAP03(2026)081

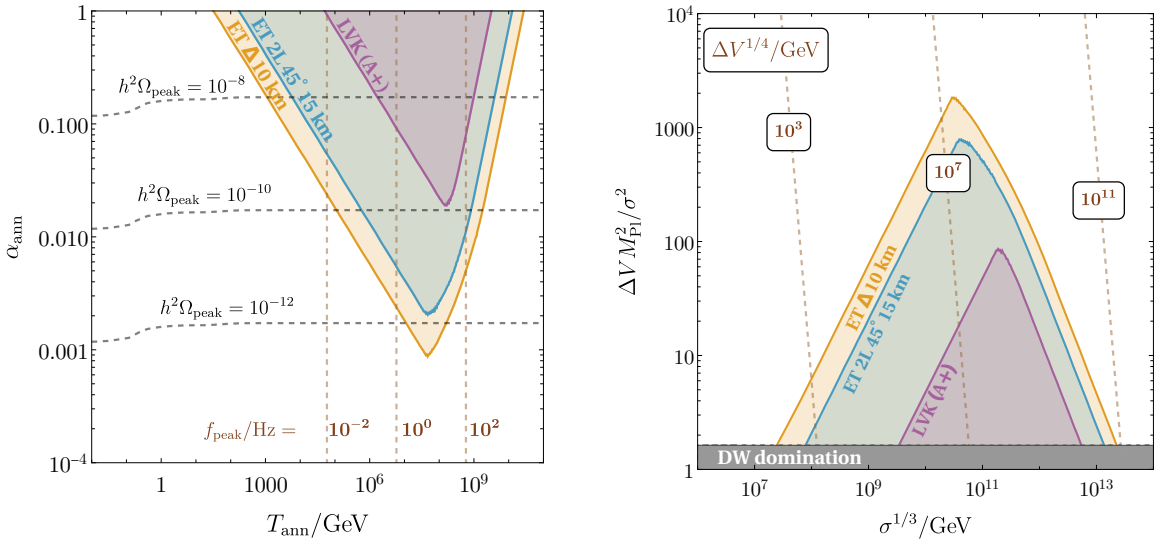

Figure 36. *Left:* $(\alpha_{\rm ann}, T_{\rm ann})$ parameter space which can be probed by ET, assuming a triangular xylophone configuration with 10km arms (orange), a 2L misaligned configuration with 15km arms (blue), both for an observation time of $T = 1$ year and SNR $= 1$. For comparison, we show the sensitivity region of LVK A+ (purple) with $T = 1$ year and SNR $= 1$. Contours of $h^2\Omega_{\rm peak}$ and $f_{\rm peak}$ are shown by black and brown dashed lines respectively. *Right:* bias vs. tension parameter space with similar sensitivity regions as on the left plot. Brown dashed lines indicate the size of the bias. The gray region corresponds to a forbidden DW dominated Universe, for which $\alpha_{\rm ann} \geq 1$.

As expected, the GW amplitude scales like $\alpha_{\rm ann}^2$ while the peak frequency is set by the correlation length of the network just before annihilation begins, which for the scaling solution corresponds to the Hubble horizon at $T_{\rm ann}$.

Figure 36 shows the reach of ET to these signals, in terms of the model independent parameters, $\alpha_{\rm ann}, T_{\rm ann}$, and of the parameters in the minimal Z_2 model. We choose to show the energy scales associated to the DW tension and the bias, $\sigma^{1/3}$ and $(\Delta V)^{1/4}$, which in the simplest model mark the scales of spontaneous and explicit breaking of the Z_2 symmetry. The breadth of the ranges of scales is remarkable.

It is worth mentioning that GWs are actually continuously radiated by the DW network from the moment of its formation. However, since the DW energy density grows with time with respect to the critical density, the contribution to the GW spectrum is maximal at $T = T_{\rm ann}$ and it outshadows the previous emission. Let us also mention that our expressions for the amplitude and peak frequency correspond to the spectrum coming from the last moment of scaling, and does not include the contribution from the actual collapse of the network. This has been recently investigated in refs. [975, 976], see also [977–979]. Additional effects may arise if the friction from the thermal plasma on the DW network is not negligible around the time of annihilation, [964, 965].

Finally, note that collapsing DW networks also can lead to substantial PBH formation, see section 3.2.5.3. This adds signatures to the DW models that are correlated with GW observables, which should be useful to discriminate among different candidate sources.

JCAP03(2026)081

3.2.5 Primordial black holes

Primordial Black Holes (PBHs) can form in the very early Universe through a variety of mechanisms and have been studied as a possible candidate to explain the dark matter (see e.g., [980] for a recent review). Nevertheless, even if they accounted for a subdominant contribution to the current energy density in the Universe, they could have played a crucial role in the cosmological history, leading to various GW signatures. As the mass of these objects is linked by model-dependent $\mathcal{O}(1)$ factors to the mass of the Hubble scale at formation, they could have formed within a very large range of masses, potentially even lighter than $m_{\rm PBH} \lesssim 10^{-18} M_\odot$ corresponding to unstable objects through Hawking evaporation within a timescale comparable to the age of the Universe [981]. The Einstein Telescope has the opportunity to constrain this putative population of BHs by searching for the associated GW signatures.

A population of PBHs is expected to form binaries which could merge in the relatively late-time Universe and lead to GWs signatures.[19] These signatures of PBH binaries falling within the ET frequency band would come from PBH of masses around the stellar mass and thus need to be distinguished from the expected signatures of astrophysical origins, i.e. coming from stars and astrophysical black holes. This is discussed in detail in chapter 4, dedicated to GW population studies.

In this section, instead, we will focus on the truly cosmological signatures of PBH formation scenarios, i.e., the cosmological GWB associated with the physical mechanisms that lead to the collapse of large overdensities in the early Universe. As the formation of PBHs requires extreme overdensities, it is generically associated with the emission of sizeable GWB. To gain an intuition on the typical mass range probed by ET, we can consider the relation between the present-day GW frequency and the mass contained in the Hubble sphere at Hubble crossing time (taken to be a proxy for the PBH mass)

$$f_{\rm GW} = 4.1\,{\rm Hz} \left(\frac{\kappa}{2.51}\right) \left(\frac{g_*}{106.75}\right)^{-1/12} \left(\frac{M_H}{10^{-17} M_\odot}\right)^{-1/2}, \tag{3.56}$$

where $\kappa = k r_m$ relates the perturbation size r_m (see, e.g., [983]) to the wavenumber k and g_* is the number of effective degrees of freedom in the energy density (see, e.g., [60, 537]), that in eq. (3.56) has been normalized to the value that it has in the Standard Model at high energy. From this relation, we immediately see that ET will probe the formation of ultra-light PBHs, potentially narrowing the open window where no bounds prevent PBHs from being the dark matter (see, e.g., [535] for a recent review).

3.2.5.1 PBHs from primordial perturbations. The simplest formation scenario assumes the collapse of extreme inhomogeneities during the radiation-dominated era [984–987]. The PBH mass resulting from the collapse is related to M_H by an order-unity factor controlled by the critical collapse parameters [988] (see [989] for a recent review). Adopting threshold

[19] Note, however, that for PBHs formed at the early Universe, the expansion of the Universe cannot be neglected, questioning the choice of metric that most adequately describes PBHs. The choice of the appropriate metric will have implications for the conditions for two PBHs to form a decoupled binary, and therefore for calculating the merger rate [982].

JCAP03(2026)081

statistics, we compute the mass fraction β assuming Gaussian primordial curvature perturbations (see e.g., [990–995] for extensions alleviating this assumptions) and accounting for the nonlinear relationship between curvature and density perturbations [996–998]. One obtains

$$\beta = \mathcal{K} \int_{\delta_l^{\min}} \mathrm{d}\delta_l \left(\delta_l - \frac{3}{8}\delta_l^2 - \delta_c\right)^{\gamma} P_{\mathrm{G}}(\delta_l)\,, \tag{3.57}$$

where P_{G} is the Gaussian distribution for the linear component of the density contrast δ_l, related to the primordial curvature perturbations by $\delta_l = -4r\partial_r\zeta(r)/3$. We indicate with $\sigma(r_m)$ the variance of the linear density field computed at horizon crossing time and smoothed on a scale r_m (see e.g., [999] for more details), while δ_c is the threshold for collapse derived by dedicated numerical relativity simulations [1000–1003]. We also introduced the parameters $\mathcal{K}$ and γ to include the effect of critical collapse [988, 1004–1007].

The same large adiabatic perturbations required in this scenario of PBH formation are also inevitably responsible for the GW emission at second order in perturbation theory [1008–1015]. The current energy density of these scalar-induced GWs (SIGW, whose effect on anisotropies of the CGWB we already discussed in section 3.1.2.1) is given, in terms of the curvature power spectrum $\mathcal{P}_\zeta$, by (see e.g., [1016] for a recent review)

$$\Omega_{\mathrm{GW},0} = c_g\,\Omega_{R,0} \int_0^\infty \mathrm{d}v \int_{|1-v|}^{1+v} \mathrm{d}u \mathcal{T}(u,v)\mathcal{P}_\zeta(ku)\mathcal{P}_\zeta(kv). \tag{3.58}$$

We introduced the parameter c_g, which accounts for the suppression of SIGW amplitude induced by the evolution of the degrees of freedom in thermal equilibrium, with $c_g \simeq 0.4$ assuming that the Standard Model remains valid up to the relevant energy, while $\mathcal{T}(u,v)$ is the so-called transfer function [1017, 1018] which accounts for the time evolution of the source. For a sufficiently narrow spectrum of curvature perturbations, the SIGW spectrum features a low-frequency tail that scales as $\Omega_{\mathrm{GW}} \sim f^3$, due to the causality limited efficiency of the super-Hubble emission [1019–1023], while the high-frequency tail that depends on the drop-off of the curvature spectrum. The peak amplitude is expected to be $\Omega_{\mathrm{GW}} \simeq 10^{-5}A^2$, where A parametrizes the enhanced amplitude of $\mathcal{P}_\zeta$ at small scales.

In figure 37, we show the region of parameter space that ET will be able to constrain by searching for SIGW signals (orange dashed line). This plot assumes the curvature power spectrum to feature a lognormal enhancement at around k_* with a width $\Delta = 1$ (see [769] for more details). The green curve indicates the amplitude required to generate PBH abundance that saturates the current constraints in the mass range shown in the upper edge of the plot.

The parameter space on the left of the dashed diagonal line in figure 37 (see also the range between the dashed lines in figures 38 and 39) indicates the asteroid mass window where the PBHs can constitute all of dark matter. For lower masses, i.e., to the right side of the dashed line, Hawking evaporation leads to the emission of particles that could be detected with different probes (mainly BBN, CMB anisotropies and distortions and cosmic rays, among others [535]). However, these bounds may be avoided in scenarios where black hole evaporation deviates from the semi-classical result [1024–1027]. Furthermore, microscopic horizonless relics could form in the early Universe either directly through gravitational collapse or as stable remnants of the Hawking evaporation of primordial black holes. In both cases they completely or partially evade cosmological constraints arising from Hawking evaporation

JCAP03(2026)081

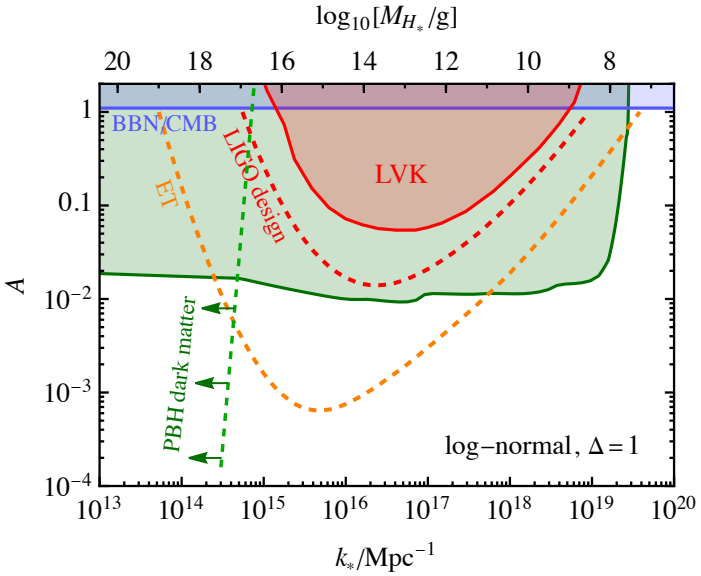

Figure 37. Upper bound on the amplitude of the curvature power spectrum at small scales A as a function of the wavenumber k_* in case of null detection of a SIGW. The green and blue regions at the top show, respectively, the exclusions from PBH constraints and from BBN/CMB constraint on the number of relativistic degrees of freedom. In red the bound from LVK is shown for comparison. Adapted from [769]. Reprinted figure with permission from [769], Copyright (2022) by the American Physical Society.

and they could still explain the entirety of the dark matter in certain mass ranges, a scenario that will be tested by ET [536, 1028, 1029].

3.2.5.2 PBHs from phase transitions. Cosmological phase transitions are typically associated with the breaking of global or local symmetries in a process where the vacuum expectation value of a scalar field changes. They can be either continuous transitions where the scalar field rolls down to the new minimum or first-order transitions that proceed by nucleation and expansion of bubbles inside which the field is in the true vacuum, see the discussion in section 3.2.2. Either way, the transition can lead to the formation of large inhomogeneities, GWs and even PBHs. For the latter, the transition typically needs to be so strongly supercooled that the vacuum energy of the scalar field in the false vacuum causes a period of thermal inflation. The formation of PBHs can occur during the transition in collisions of several bubbles [1030–1032] or after it when the scales that exited the cosmological horizon during the thermal inflation reenter the horizon [1033–1037]. In terms of the phase transition parameters defined in section 3.2.2, the first-order phase transitions where PBH formation is efficient correspond to $\alpha \gg 1$ and $\beta/H_* \lesssim 8$.

In case of a first-order phase transition, the distribution of the density contrast δ generated for the modes that exited horizon during the thermal inflation has a negative non-Gaussianity [1037]. For comparison, models of primordial inflation including an ultra-slow-roll period during which the fluctuations can became very large predict a positive non-Gaussianity [1038]. This implies that the SIGW signature (3.58) of the PBH formation from fluctuations generated during a first-order phase transition is stronger because the

JCAP03(2026)081

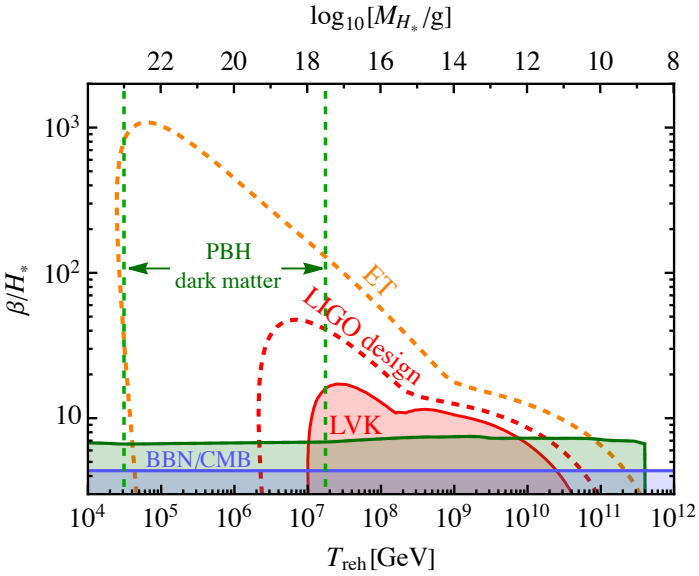

Figure 38. Lower bound on the inverse time duration of the phase transition β/H_* as a function of the temperature $T_{\rm reh}$ right after the phase transition in case of null detection of a SIGW. The green and blue regions at the bottom show the exclusions from PBH constraints and from BBN/CMB constraint on the number of relativistic degrees of freedom.

PBH abundance is sensitive to the large δ tail of the distribution that is suppressed by the negative non-Gaussianity, whereas the SIGW abundance is sensitive to the typical values of δ, i.e. the width of the distribution. Moreover, as discussed in section 3.2.2, also the bubble collisions source GWs. Consequently, the GW spectrum related to PBH formation in a strongly supercooled first-order phase transition has two peaks [1037]: the SIGW peak at the scale corresponding to the horizon size at the end of the thermal inflation, and the bubble collisions GW peak at the scale corresponding to the typical bubble size.

In figure 38 we show the parameter space ET will be able to probe by searching the GWB from a strongly supercooled ($\alpha \gg 1$) first-order phase transition. For $\beta/H_* \lesssim 20$ the double-peak structure of the spectrum can be detectable, whereas for $\beta/H_* \gtrsim 20$ the component sourced by bubble collisions fully dominates the spectrum. The range of ET extends up to PBH masses $\simeq 10^{-10}\,M_\odot$, covering the asteroid mass window where PBHs can constitute all DM. At these masses ET will probe the high-frequency tail of the GW spectrum sourced by the bubble collisions.

3.2.5.3 PBHs from collapsing domain wall networks. We have summarized the motivation and observational consequences of Domain Walls in section 3.2.4. In short, DW networks have a strong impact on cosmology and so they are an excellent means to probe models with spontaneously broken discrete symmetries. The strong impact translates into abundant production of cosmological relics, like a GW background.

The ability of DW networks to form PBHs has been re-examined recently [976, 1039–1046]. The PBH formation process is tied to the annihilation regime, the end of the DW epoch. As in section 3.2.4, we specialize the discussion to the simplest annihilation mechanism, a small explicit breaking of the discrete symmetry. This uplifts the degeneracy in the vacuum

JCAP03(2026)081

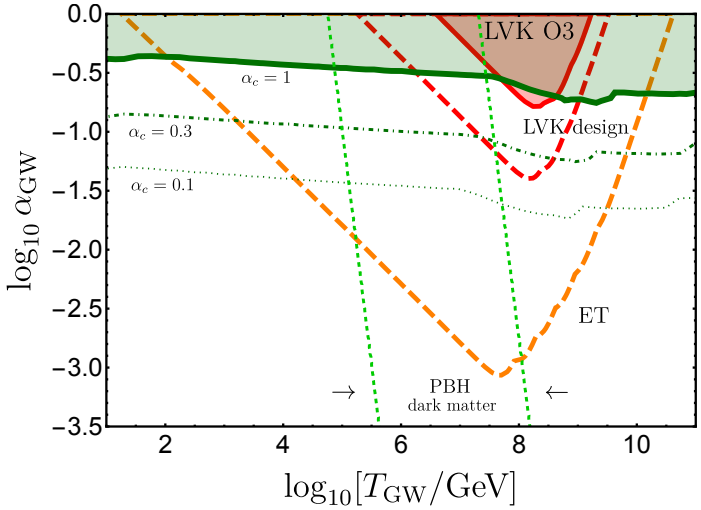

Figure 39. Constraints from PBH overproduction as a function of temperature $T_{\rm GW}$ and DW abundance at the peak of GW emission (adapted from [976]). Superimposed, the detectable regions with ET and LKV design as well as the exclusion from LVK O3 data. The shaded region above the solid line is excluded from the PBHs formed at $t_{\rm PBH}$ or later. The dash-dotted and dotted lines refer to sub-Hubble PBHs, for representative values of α_c, giving a reasonable sense of current systematic uncertainties. The vertical dashed lines indicate the asteroid mass range (assuming $\alpha_c = 1$). Reproduced from [976]. The Author(s). CC BY 4.0.

energies of the vacua, ΔV, which acts as a pressure that pushes the walls to increase the true vacuum volume. During annihilation most DWs collapse due to tension $\sigma_{\rm DW}$ and vacuum difference ΔV. The annihilation time $t_{\rm ann}$ is estimated from $\sigma_{\rm DW} H_{\rm ann} \simeq \Delta V$. At that time the fraction in DWs is given by $\alpha_{\rm ann}$, see (3.53), which must satisfy $\alpha_{\rm ann} < 1$ in order not to run into a DW problem.

The PBH abundance is mainly governed by two factors [1042]: the likelihood that Hubble-sized false vacuum pockets shrink within their own Schwarzschild volume R_S^3; and the number of Hubble-sized pockets at each time. The first factor is small at $t_{\rm ann}$ (for $\alpha_{\rm ann} \ll 1$), but it increases in time [1042]. This leads to a rather sharp notion of 'PBH formation time', $t_{\rm PBH}$, defined as when the Schwarzschild radius of a Hubble-sized pocket coincides with the Hubble length. Surviving Hubble-sized pockets at $t \gtrsim t_{\rm PBH}$ convert into BHs efficiently, independently of shape and angular momentum (and have a baby-Universe wormhole topology, see [1039, 1040]). Notice that there is a parametric delay between the time of GW emission (set by $t_{\rm ann}$ up to a numerical factor [976]) and PBH formation: $t_{\rm PBH} \sim t_{\rm GW}/\alpha_{\rm ann}^{1/2}$ [976, 1042].

The second factor (the abundance of Hubble sized pockets) requires a dedicated computation of how fast the network decays in time, which is challenging from the point of view of numerical simulations. Recent work combining numerical simulations and semi-analytical methods [976] concluded that this abundance decays like $\exp\left[-(t/\tau)^{3/2}\right]$, see also [1047]. For Hubble-sized pockets the decay time τ is shorter than $t_{\rm ann}$ by a factor $2-3$ [976]. This leads to a very strong dependence of the abundance, of the form $\exp\left[-c\,\alpha_{\rm ann}^{-3/4}\right]$ with c a constant.

False vacuum pockets entering before $t_{\rm PBH}$ can also form BHs, though they require some amount of sub-Hubble contraction. Their collapse probability depends significantly

JCAP03(2026)081

on asphericities, angular momentum, etc, but on the other hand these pockets are more abundant. A proper computation of this population is challenging and, at present, lacking. A pragmatic way to account for these sub-Hubble BHs is to introduce a lower collapse criterion, α_c (the minimum value of $R_S H$ when the pocket enters the Horizon).

The resulting constraints are shown in figure 39 as a function of temperature $T_{\rm GW}$ and DW abundance at the peak of GW emission, together with the detectable regions in ground based observatories. Remarkably, ET will be able to test whether DM is composed of asteroid mass PBHs produced during the collapse of a DW network.

3.2.6 GWs as probes of the early Universe expansion history

When studying modifications to the standard cosmological model based on GR and ΛCDM, it is convenient to distinguish between the early Universe evolution, defined as the evolution from the earliest instants of the Universe until, say, Big Bang Nucleosynthesis (BBN), and the late Universe evolution, from BBN until the present epoch. The late Universe evolution is strongly constrained by observations, and the role of GWs in probing it will be discussed in details in section 3.3. Early Universe cosmology is much less constrained. Deviations from the predictions of GR and ΛCDM could appear as a consequence of modifications of gravity relevant at high energies, which indeed emerge in different contexts [1048], such as scalar-tensor theories [1049–1051], braneworld theories [1052, 1053], compactified extra dimensions and Kaluza-Klein models [1054, 1055], $f(R)$ theories and theories with higher-order terms in the curvature invariants [1056, 1057], string loop effects [1058] or string cosmology [695, 1059]. The evolution predicted by the standard ΛCDM cosmological model can also be affected, in the early Universe, by physics beyond the Standard Model, phase transitions, etc. In the previous subsections we have seen for instance how such physics beyond the Standard Model could lead to GW signals produced by cosmic strings, domain walls, or related to primordial BH formation.

Another way in which GWs can be used to probe the early Universe, and in particular modifications of its expansion history, is through the imprint that the expansion history leaves on primordial GWs (PGWs) produced in the early Universe, as they propagate until the present epoch. This information is contained in the transfer function, that connects the primordial power spectrum to the power spectrum observed today. To fix the notation, let us recall that the primordial power spectrum $\mathcal{P}_{T,\rm in}(k)$ of the tensor perturbations was defined in eq. (3.33). The simplest form of the spectrum, at least in a range of comoving wavenumbers k close to a "pivot scale" k_*, is just a power-law, see eq. (3.34), characterized by an amplitude A_T (which depends on the value chosen for k_*) and a tilt n_T (which to a first approximation can be taken as constant, or else can also be made to "run" with k). A typical choice for k_* is $0.05\,\mathrm{Mpc}^{-1}$, corresponding to the wavenumbers probed by the CMB. The tensor amplitude $A_T(k_*)$ can be traded for the tensor-to-scalar ratio $r(k_*) = A_T(k_*)/A_S(k_*)$, where $A_S(k_*)$ is the analogous amplitude for scalar perturbations, whose value is fixed by CMB observations: e.g., $A_S(k_* = 0.05\,\mathrm{Mpc}^{-1}) \simeq 2.14 \times 10^{-9}$.

Given a cosmological model, such as ΛCDM, the evolution in time of the Fourier modes of the GW perturbations over a FRW background can be computed, and the result is encoded

JCAP03(2026)081

in the transfer function $T_{\rm GW}(k)$,

$$\tilde{h}_A(\eta_0, k) = T_{\rm GW}(k)\tilde{h}_A(\eta_{\rm in}, k)\,, \tag{3.59}$$

(where $A = +, \times$ labels the two polarizations and, at least in GR as well as in any modifications of it that preserves parity, the transfer function is the same for both polarizations). Then, the power spectrum observed today, $\mathcal{P}_{T,0}(f)$, is related to the primordial tensor power spectrum by

$$\mathcal{P}_{T,0}(k) = |T_{\rm GW}(k)|^2\,\mathcal{P}_{T,{\rm in}}(k)\,. \tag{3.60}$$

Instead of the comoving wavenumber k, we can equivalently express all results in terms of the GW frequency observed today, f, which (in units $c = 1$) is related to k by $f = k/(2\pi)$. The relation between $\Omega_{\rm GW}(f)$ and $\mathcal{P}_{T,0}(k)$ is given by [see eq. (19.288) of ref. [60]]

$$\Omega_{\rm GW}(f) = \frac{\pi^2}{3H_0^2}\,f^2\mathcal{P}_{T,0}(f)\,, \tag{3.61}$$

and therefore

$$\Omega_{\rm GW}(f) = \frac{\pi^2}{3H_0^2}\,f^2|T_{\rm GW}(f)|^2\,\mathcal{P}_{T,{\rm in}}(f)\,, \tag{3.62}$$

where we have used $f = k/(2\pi)$ as the argument of the functions. In particular, for modes that re-entered the horizon during radiation dominance, i.e. modes with $f \gg f_{\rm eq} \sim 1.7\times10^{-17}\,{\rm Hz}$ (and therefore for modes relevant for pulsar timing arrays, space-borne and ground based GW interferometers), we have

$$h_0^2\Omega_{\rm GW}(f) \simeq \frac{1}{24}\,h_0^2\Omega_{\rm R}\,\left(\frac{g_*(T_k)}{3.363}\right)\left(\frac{3.909}{g_*^S(T_k)}\right)^{4/3}\,\mathcal{P}_{T,{\rm in}}(f)\,, \tag{3.63}$$

where $\Omega_{\rm R}$ is the energy fraction of radiation (numerically $h_0^2\Omega_{\rm R} \simeq 4.184\times10^{-5}$); T_k is the temperature at which a mode with comoving wavenumber k re-enters the horizon; and $g_*(T)$ and $g_*^S(T)$ are the effective number of species in the energy density and in the entropy, respectively, at temperature T. For the frequencies relevant for space-borne and ground-based interferometers we have $T_k \gg 100\,{\rm GeV}$ and, in the Standard Model, $g_*(T_k) = g_*^S(T_k) \simeq 106.75$, and therefore

$$h_0^2\Omega_{\rm GW}(f) \simeq 6.73\times10^{-7}\,\mathcal{P}_{T,{\rm in}}(f)\,, \tag{3.64}$$

where we have used the numerical value $h_0^2\Omega_{\rm R} \simeq 4.184\times10^{-5}$. Equivalently, using eq. (3.34) for the primordial power spectrum, and writing $A_T(k_*) = r(k_*)A_S(k_*)$, $h_0^2\Omega_{\rm GW}(f)$ can be written as in eq. (3.35).

If the cosmological evolution is modified, with respect to that obtained assuming the validity of GR and ΛCDM, the transfer function in eq. (3.59) will be different and, given a mechanism that produces a known primordial spectrum $\mathcal{P}_{T,{\rm in}}(f)$, the stochastic GW background observed today, given by eq. (3.62), will be different from that expected in GR and ΛCDM. Stochastic GW backgrounds can therefore be a probe of the expansion history of the Universe, and in particular of the early Universe, for which it is in general more difficult to obtain observational constraints.

JCAP03(2026)081

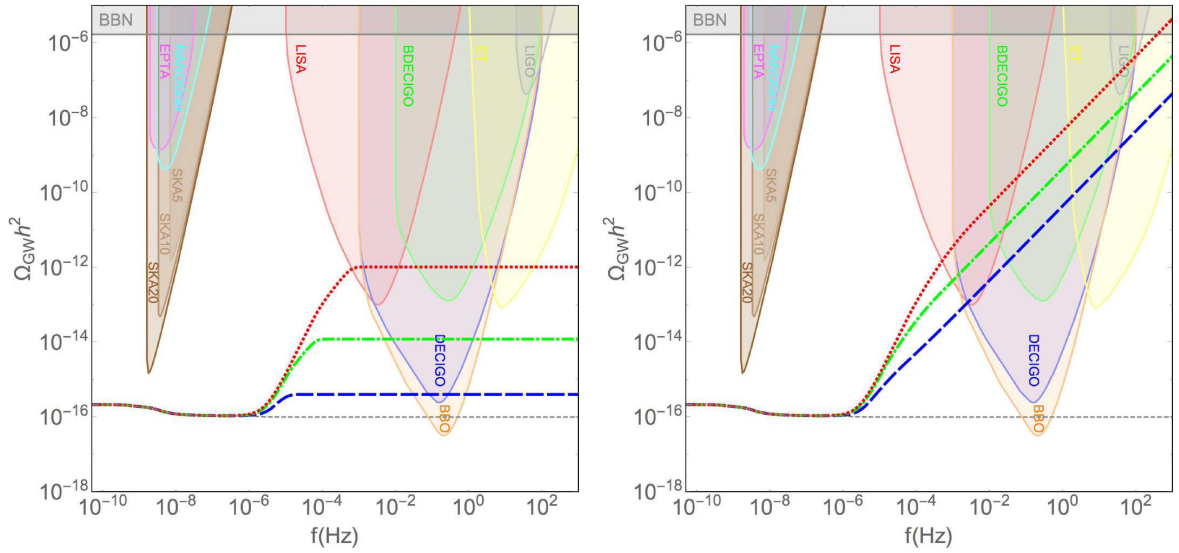

Figure 40. $h^2\Omega_{\rm GW}(f)$ for the amplification of vacuum fluctuations in standard single-field slow-roll inflation. The gray dashed lines corresponds to the result in GR+ΛCDM, assuming a tensor-to-scalar ratio $r = 0.07$ and a scale-invariant primordial tensor spectrum, $n_T = 0$. The colored lines show the result obtained with the modified cosmological discussed in the text, for fixed $f_* \simeq 2.5 \times 10^{-6}$ Hz, and $A_* = 1$ (blue dashed lines), $A_* = 10$ (green dot-dashed lines), $A_* = 100$ (red dotted lines), and $\nu = 0$ (left panels), $\nu = 1$ (right panels). The colored regions refer to the BBN constraint and the projected sensitivities of various GW observatories. Reproduced from [1066], © 2020 IOP Publishing Ltd and Sissa Medialab. All rights reserved.

Power-like phenomenological modifications of the expansion rate. At the level of background evolution, modification of the expansion rate can be described writing $H(t)$ as $H_{\rm MC}(T) = A(T)H_{\rm GR}(T)$ [1060–1062], where $H_{\rm MC}(T)$ refers to a given modified cosmology while $H_{\rm GR}(T)$ refers to the standard cosmological model (GR+ΛCDM). The factor $A(T)$, which depends on the temperature and accounts for the underlying modified cosmological model, can be parameterized phenomenologically in different ways [1060, 1061]. In all cases, to avoid conflict with the successful predictions of BBN [1063–1065], the parametrization must satisfy the conditions $A(T) \to 1$ at the onset of the BBN period. At early times, however, one can have $A(T)$ significantly different from one. A number of models, in this regime, can be described by a power-law function $A(T) \simeq A_*(T/T_*)^\nu$ [1060, 1061], with $\{A_*, \nu\}$ dimensionless constants and T_* a reference temperature. In particular, $\nu = 2$ corresponds to a Randall-Sundrum type II brane cosmology; $\nu = 1$ to kination models in GR; $\nu = 0$ gives a model with a constant rescaling of the Hubble expansion rate; $\nu < 0$ in scalar-tensor cosmology; and $\nu = 2/n - 2$ in $f(R)$ cosmology, with $f(R) = R + \alpha R^n$. This power-law behavior is then smoothly interpolated toward $A(T) = 1$ at some temperature T_* [1060, 1061]. For the analysis of the PGWs spectrum, it is convenient to refer to the frequency f_*, instead of the corresponding temperature T_*. For $f \ll f_*$ and $f \gg f_*$, the following general cases can be analyzed [1066, 1067]:

- $f \ll f_*$. In this range of frequencies, the cosmology converges to GR, $H(a) = H_{\rm GR}(a)$, so the transfer function is the same and, for a given primordial spectrum $\mathcal{P}_{T,\rm in}(f)$, the

JCAP03(2026)081

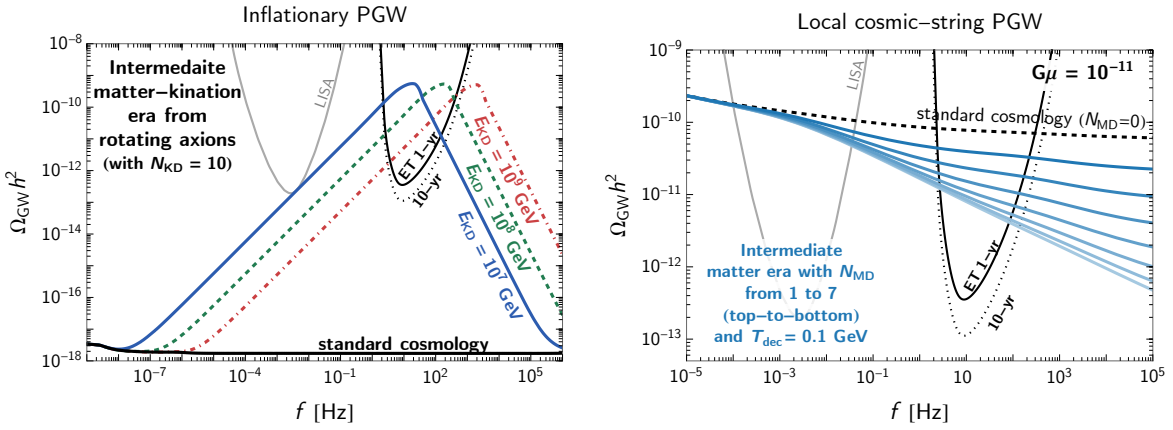

Figure 41. (left) Inflationary spectra induced by the intermediate matter-kination era are shown as colored lines, while the prediction from standard ΛCDM cosmology is the black line. Following the period of matter domination, the intermediate kination era starts at energy scale $E_{\rm KD}$ and lasts for $N_{\rm KD}$ e-folds of the scale-factor expansion. We assume the scale invariant tensor perturbation with inflationary energy scale $E_{\rm inf} \simeq 1.6 \times 10^{16}$ GeV. The sensitivity curves of ET assume respectively 1 and 10 years of observation with SNR = 1, and the LISA sensitivity comes from [647]. (right) Effect of an intermediate matter era — lasting for $N_{\rm MD}$ efolds and ending at temperature $T_{\rm dec}$ — on the prediction for $h^2\Omega_{\rm GW}(f)$ from local cosmic strings, shown by the blue lines [871, 1067–1069]. Reproduced from [1067], © 2020 IOP Publishing Ltd and Sissa Medialab. All rights reserved.

spectrum $\mathcal{P}_{T,0}(f)$ observed today is the same. Therefore $h_0^2\Omega_{\rm GW}(f) \propto \mathcal{P}_{T,\rm in}(f)$, see eqs. (3.63) and (3.64).

- $f \gg f_*$. In this range of frequency, the factor $A(f)$ plays a major role. The regimes where $\nu > 0$, $\nu = 0$, and $\nu < 0$ are separately discussed:

  – $\nu > 0$: if ν takes positive values, the PGW relic density reads $\Omega_{\rm GW}(f) \propto \mathcal{P}_{T,\rm in}(f)\, f^{\frac{2\nu}{1+\nu}}$, in which appears an extra factor $f^{\frac{2\nu}{1+\nu}}$, that generates a blue-tilted modification to the original tensor power spectrum. This enhancement follows from the reduction of the friction term entering the equation of GWs.

  – $\nu = 0$: In this case, the Hubble rate is enhanced by a constant factor $A = 1 + A_*$, and the PGW spectrum is therefore not distorted and is modified by an overall shift $\Omega_{\rm GW}(f) \propto (1 + A_*)^2 \mathcal{P}_{T,\rm in}(f)$.

  – $\nu < 0$: for negative values of ν, the factor $A \to 1$ both for low ($f \ll f_*$) and high frequencies ($f \gg f_*$), with a maximum at $f = \bar{f} \gtrsim f_*$ given by $A(\bar{f}) = A_*$. In these limits the PGW spectrum presents the same tilt as the original tensor power spectrum, with a characteristic bump at $f = \bar{f}$.

Figure 40 shows $h^2\Omega_{\rm GW}(f)$ for the amplification of vacuum fluctuations in standard single-field slow-roll inflation. The result in GR+ΛCDM is given by the gray dashed line, while the colored lines shows the results for $\nu = 0$ (left panel) and $\nu = 1$ (right panel) for different values of A_*. The colored regions refer to projected sensitivities for different GW experiments.

JCAP03(2026)081

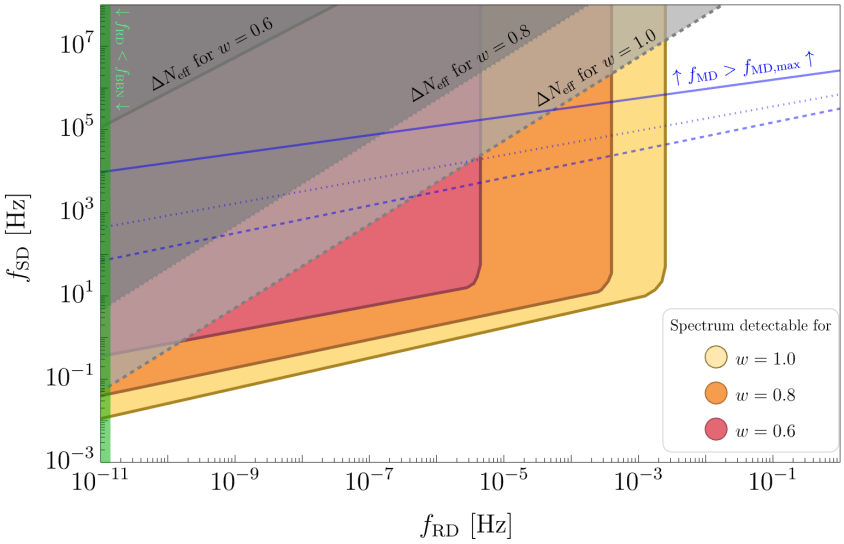

Figure 42. The $(f_{\rm RD}, f_{\rm SD})$ parameter regions accessible by ET are shown. The colored regions represent the detectable parameter spaces for three different values of w: red for $w = 0.6$, orange for $w = 0.8$, and yellow for $w = 1.0$ (corresponding to kination). The gray regions indicate the parameter space excluded by indirect limits from BBN and CMB, with the darkest gray for $w = 0.6$ and the lightest gray for $w = 1$. We again assume the scale invariant tensor perturbation with inflationary energy scale $E_{\rm inf} \simeq 1.6 \times 10^{16}\,{\rm GeV}$. The parameter $f_{\rm MD}$ is chosen as a function of $f_{\rm RD}$, $f_{\rm SD}$ and w, as described in the text, and we denote the parameter region where $f_{\rm MD} > f_{\rm MD,max}$ with blue lines (dashed for $w = 1$, dotted for $w = 0.8$ and thick for $w = 0.6$). The sensitivity curve of ET assumes 1 year of observation with SNR = 1. The green area on the left is excluded, since there $f_{\rm RD} < f_{\rm BBN}$, which is not allowed. Reprinted figure with permission from [1074], Copyright (2024) by the American Physical Society.

Modified equation of state in the early Universe. As another example of modified expansion history, if there were some pre-BBN epochs in the cosmological history with a modified equation of state associated for instance with either a matter domination or a stiff era, this would lead to a tilt in $\Omega_{\rm GW}(f)$ with spectral index $\beta = -2(1-3w)/(1+3w)$, with w the equation of state of the Universe, at the frequencies corresponding to the modes which re-entered the horizon in this non-standard era [1062, 1070, 1071]. For example, the kination era right after inflation can result in the enhanced GW spectrum shown in the right panel of figure 40, although any observable signal at ET would be strongly constrained by $\Delta N_{\rm eff}$ bound, as shown in [1070, 1071]. The most striking case comes from an intermediate matter-kination era, well-motivated by rotating axions [1071–1073], that largely amplifies the inflationary signal and induces the "triangular signature" [with $\beta = 1$ during kination era ($w = 1$) and $\beta = -2$ slope during matter era ($w = 0$)] shown in the left panel of figure 41. This amplification can make the signal from slow-roll inflation observable at ET, for kination energy scales of order $(10^6 - 10^9)\,{\rm GeV}$, that connect to axion mass m_a and axion decay constants f_a in the range $m_a \lesssim 6.5\ \mu{\rm eV}(10^9\,{\rm GeV}/f_a)(\Omega_a/\Omega_{\rm DM})$, where the last bracket is the energy fraction of axions as dark matter [1071].

JCAP03(2026)081

Furthermore, one can study scenarios with a stiff epoch weaker than kination ($1/3 < w < 1$) [1070, 1074]. As a case study, we focus on a cosmological history similar to the one studied above, where after inflation there is an intermediate radiation-matter-stiff era (denoted with RD1, MD and SD respectively), followed by the conventional radiation dominated Universe. We assume instantaneous transitions between the different epochs. This scenario also leads to a peak-like spectrum that can be testable at Advanced LIGO A+ sensitivity and by third-generation detectors [1074]. The frequency of the stiff-to-radiation transition is denoted by $f_{\rm RD}$, and the one of matter-to-stiff transition by $f_{\rm SD}$. The parameter space of the model that is testable at ET is illustrated in figure 42, for three different values of the equation of state w during the stiff period. Assuming no entropy variation, the frequency at the RD1-to-MD transition can be expressed as $f_{\rm MD} = f_{\rm RD}^{\frac{1-3w}{1+3w}} f_{\rm SD}^{\frac{6w}{1+3w}}$. This transition cannot occur earlier than the end of inflation, implying a maximum value of $f_{\rm MD,max} = 1.8 \times 10^8\,{\rm Hz}$. This limit is indicated by the blue lines in figure 42.

The non-standard era beyond the radiation era at high temperatures not only impact the inflationary PGW, but it can also lead to significant spectral distortions in GW from other cosmological sources, in particular, from cosmic strings [870–872, 1068, 1069, 1071, 1073, 1075–1077], and causality tails [828, 1021, 1071, 1078, 1079]. The frequencies at which the spectral slope gets modified correspond to the scales at which the GW is being produced; the slope depends on the equation of state of the Universe and can differ from the case of inflationary PGW; see e.g., [1062, 1080] for reviews. This is illustrated for the case of local cosmic strings in the right panel of figure 41.

Oscillation features in the GWB. Interferometers such as ET have the capability not only to observe the general coarse-grained trend of a primordial GWB, but also its fine-grained features. In particular, periodic oscillatory patterns in the GWB have been identified as distinctive signatures of primordial features [1081–1083]. These imprints reflect early-universe dynamics that deviate significantly from scale invariance and arise across a broad range of theoretical frameworks, including both inflationary models and their alternatives (see [1084–1086] for reviews on the subject). The GWB provides a powerful observational probe of primordial features at scales well beyond the reach of the CMB and galaxy surveys, where most searches have traditionally been concentrated. Detecting such signatures would unveil new physics beyond the standard cosmological model and opening an unprecedented window into the dynamics of the primordial universe.

Primordial features often manifest as oscillations in the scalar power spectrum. These have been found to be of two types. *Sharp features* arise from brief deviations in background parameters from their attractor behavior, producing transient, linear oscillations in the scalar power spectrum. This linear oscillatory shape typically appears in inflationary models with a step-like feature in the potential [1087–1096], turns in the multi-field trajectory [1091, 1097–1100] or sudden transition in the speed of sound [1101–1104]. *Resonant features* result from periodic background oscillations that resonate with quantum modes of the primordial curvature fluctuations, leading to sustained oscillations at constant frequency across a wide log-scale range. These log-oscillations can be produced in inflationary scenarios where the inflaton potential has oscillatory bumps [1105], multi-field dynamics [1091, 1106–1111],

JCAP03(2026)081

other settings such as axion monodromy inflation [1112–1115] and axion Chern-Simons gravity [1116]. A hybrid of both types appears in models known as classical primordial standard clocks [1106, 1107, 1110, 1111, 1117–1127].

These features in the scalar sector are imprinted in the GWB through nonlinear interactions [1081–1083, 1100, 1128, 1129], where scalar perturbations source tensor modes, if their amplitude is sufficiently large. A broad class of oscillatory patterns in the GWB can then be captured by the following generic templates, either of linear oscillations,

$$\Omega_{\rm GW}(f) = \bar{\Omega}_{\rm GW}(f) \left\{ 1 + \sum_{l=1}^{l_{\rm max}} \left[A_l^{\rm c} \cos\left(l\omega \frac{f}{f_*} \right) + A_l^{\rm s} \sin\left(l\omega \frac{f}{f_*} \right) \right] \right\}, \tag{3.65}$$

or of log-periodic ones,

$$\Omega_{\rm GW}(f) = \bar{\Omega}_{\rm GW}(f) \left\{ 1 + \sum_{l=1}^{l_{\rm max}} \left[A_l^{\rm c} \cos\left(l\omega \ln \frac{f}{f_*} \right) + A_l^{\rm s} \sin\left(l\omega \ln \frac{f}{f_*} \right) \right] \right\}, \tag{3.66}$$

where $\bar{\Omega}_{\rm GW}(f)$ is the envelope or main spectral shape, f is the observed frequency of the GW signal, f_* is the pivot frequency scale of the observatory, $l_{\rm max}$ denotes the maximum harmonic determined by the sourcing mechanism. The coefficients $A_l^{\rm c,s}$ represent (not necessarily constant) amplitudes, and ω is the angular frequency of the oscillations — not to be confused with the frequency f.

Sharp features during inflation lead to the template in eq. (3.65) in its simplest form, i.e. $l_{\rm max} = 1$ [1081, 1082], for GWs produced when scalar fluctuations — affected by the feature — re-enter the horizon during the post-inflationary era.[20] In this context, the characteristic frequency is $\omega \sim 2/f_{\rm f}$, where $f_{\rm f}$ corresponds to the scale that exited the horizon at the time of the feature during inflation. Typically, the resulting GW spectrum exhibits $O(10\% - 20\%)$ modulations, arising from the resonant amplification of $O(1)$-level oscillations in the sourcing scalar power spectrum. These oscillations arise from moderate to copious particle production induced by the sharp feature [1081]. This also leads to a characteristic relation between the frequency at which $\Omega_{\rm GW}$ peaks, denoted f_*, and the feature scale f_f, typically given by $f_* \sim \mathcal{O}(10\text{–}100)\, f_f$. Consequently, for a signal within the ET band, linear oscillations can be probed in the range $0.1/\text{Hz} < \omega < 10/\text{Hz}$. Additionally, both the amplitude of the oscillations and the shape of the envelope are influenced by the background equation of state at the time of GW production [1128].

Resonant features, on the other hand, lead to a template as given in eq. (3.66), with $l_{\rm max} = 2$. In this case, the GW spectrum exhibits a superposition of two oscillatory components, with frequencies $\omega_{\rm log}$ and $2\omega_{\rm log}$ [1083]. Here, $\omega_{\rm log}$ corresponds to the logarithmic oscillations in the primordial power spectrum, often linked to a mass parameter in units of the Hubble scale. The relative amplitudes of these two harmonics depend on $\omega_{\rm log}$, the shape of the peak in the scalar power spectrum, and the background equation of state at the time of GW production. The templates that have been derived in [1081–1083, 1128] for the post-inflationary contribution to the GWB encapsulate these dependencies.

[20] For the template of primordial GWs sourced directly at the time of the feature during inflation, see ref. [1130].

JCAP03(2026)081

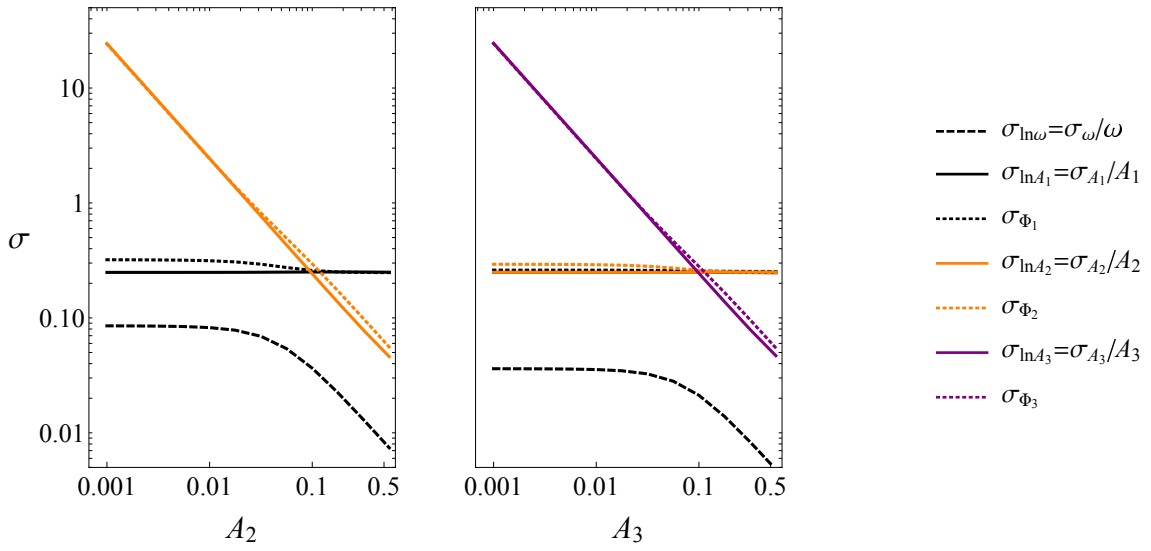

Figure 43. Dependence of the expected relative errors σ for $l_{\rm max} = 2$ (left) and $l_{\rm max} = 3$ (right) harmonics. The oscillation amplitude A_2 and A_3 vary, while the other parameters are fixed as follows. For $l_{\rm max} = 2$: $\Omega_0 = 10^{-11}$, $n_{\rm t} = 0$, $\omega = 10$, $A_1 = 0.1$, $\Phi_1 = 0$. For $l_{\rm max} = 3$: $A_2 = 0.1$, $\Phi_2 = 0$ and $\Phi_3 = 0$. The black, orange and purple curves correspond to the oscillation parameters (oscillation amplitude A_l and phase Φ_l) for $l = 1$, $l = 2$, and $l = 3$, respectively. Reproduced from [1131], © The Author(s). Published by IOP Publishing Ltd. CC BY 4.0.

The log-oscillatory profile in eq. (3.66) can also be produced directly in the tensor sector as a manifestation of a broken discrete scaling symmetry in scenarios of quantum gravity [1131, 1132]. In this case, the energy spectrum in (3.66) is given by eq. (3.63) with

$$\mathcal{P}_{T,\rm in}(k) = \bar{\mathcal{P}}_{T,\rm in}(k)\left[1 + A_1^{\rm c}\cos\left(\omega\ln\frac{k}{k_*}\right) + A_1^{\rm s}\sin\left(\omega\ln\frac{k}{k_*}\right)\right], \tag{3.67}$$

where the prefactor $\bar{\mathcal{P}}_{T,\rm in}(k)$ depends on the model. A function F is invariant under a discrete scale symmetry if $F(\lambda_\omega^m f) = F(f)$, where $\lambda_\omega := e^{\frac{2\pi}{\omega}}$ and m is an integer. The oscillatory modulation of (3.66) enjoys this symmetry but the envelope $\bar{\Omega}_{\rm GW}(f)$ in general does not. A discrete scale invariance in frequency as the one above corresponds to a symmetry in momentum space, mirrored by an invariance under discrete dilations $x^\mu \to \lambda_\omega x^\mu$ in position space. Such a micro-structure of spacetime geometry would correspond to the one of a deterministic (multi-)fractal [1133–1137] replicated at all scales. This everpresence of the same structure transcending a UV/IR divide is responsible for the appearance of log oscillations at all frequencies in (3.66).

Expressions (3.65) and (3.66) can serve as templates to fit any signal displaying linear or logarithmic oscillations, regardless of its physical origin [1131]. To check the detectability of the log oscillations in ET, in [1131] the Fisher matrix for the cross-correlation analysis was calculated to estimate the expected error on the parameters in (3.66) for the ET-D sensitivity curve assuming a three-year observation run. It has been shown that, for oscillation amplitudes $A_l \sim 0.1$ and a frequency $\omega \sim 10$, we need a detection with signal-to-noise ratio $\gtrsim 100$ to determine all the oscillation parameters with an $O(10\%)$ precision. If the GWB is

JCAP03(2026)081

primordial and the envelope is parameterized by $\bar{\Omega}_{\rm GW} = \Omega_0 (f/f_*)^{n_t}$, the minimum GWB amplitude Ω_0 and the minimum tensor tilt $n_{\rm t}$ needed to achieve such SNR at the ET frequencies satisfying the current upper bound $r < 0.036$ of the tensor-to-scalar ratio at the CMB scale $k_0 = 0.05\,{\rm Mpc}^{-1}$ [674] are roughly

$$\Omega_0 \gtrsim 10^{-11}\,, \qquad n_{\rm t} \gtrsim 0.28\,. \tag{3.68}$$

Relative errors on oscillation frequency, oscillation amplitude, and the oscillation phase scale as $\sigma_{\ln\omega} \propto 1/(A_l\omega)$, $\sigma_{\ln A_l} \propto 1/A_l$ and $\sigma_{\Phi_l} \propto 1/A_l$, respectively, and they all decrease as $\propto 1/{\rm SNR}$. Notably, the error is insensitive to the inclusion of higher-order harmonics, for the reason that oscillation frequencies are ordered hierarchically as integer multiples of ω and each term in the harmonic expansion can be constrained independently. The $l_{\rm max} = 2$ and $l_{\rm max} = 3$ cases are shown in figure 43. The range of ω accessible by ET is roughly

$$10 < \omega < 10^3\,, \tag{3.69}$$

where the lower bound is fixed by requiring to have enough oscillation cycles inside the sensitivity band of ET and the upper bound is determined by $\omega < f/\Delta f$, where Δf is the frequency resolution of the instrument. Our estimation is obtained by $f \sim 10$Hz and $\Delta f \sim 0.01$Hz, which is a similar value used in the LVK stochastic analysis as a result of coarse graining.

3.3 Probing the late Universe with Einstein Telescope

In the previous section we have discussed how ET can probe the early Universe. The relevant observable, in that case, is the stochastic GW background of cosmological origin that, as we have seen, can be generated by many different early Universe mechanisms. For probing the late Universe with GWs, in contrast, the most important signals are those due to the coalescence of compact binaries. A crucial feature of GWs for late time Universe studies is the fact that CBC sources are self-calibrating distance indicators. When the redshift of the source can also be somehow inferred, one can reconstruct the distance-redshift relation, tracking the expansion history of the Universe and constraining cosmological parameters such as the Hubble constant [1138, 1139], similarly to the use of standard candles. In this context, CBC are then called "standard sirens". This reconstruction is, however, non-trivial, since from a GW alone one can not in general infer the redshift, which is degenerate with the chirp mass. While breaking this degeneracy is possible in special cases, like for *Love sirens* [1140], or for matter structure/cosmological effects considered in [1141], in general direct redshift measurements are not possible with GW detectors. On the other hand, for *bright standard sirens*, which are those events followed by electromagnetic counterparts, direct redshift measurements are enabled by host galaxy identification. However, most GW events seen so far by LVK have not been followed by electromagnetic counterparts, hence the name of *dark (standard) sirens*. With dark sirens, the most common techniques for cosmological parameter estimation rely on combinations with galaxy catalogs from which redshift information can be extracted [1138, 1142], allowing to track the cosmic expansion history [1143–1147]. Additionally to these methods, one can make use of known merger redshift distribution [1148–1150] or features in the mass distribution of BHs and NS to obtain redshift

JCAP03(2026)081

information [1151–1157], a technique called *spectral sirens*. We highlight, however, that cosmological and astrophysical population inference are deeply intertwined [1145, 1147, 1158–1161]. In this section we discuss various types of methods for doing cosmography with ET and their prospects.

3.3.1 Cosmography with coalescing binaries

3.3.1.1 Bright sirens. Bright sirens are expected to have two main types of prompt electromagnetic counterparts: kilonova (KN) explosions, and short GRBs, as we know from the celebrated example of GW170817 [3, 4]; see section 5 for a detailed discussion of the perspective for multi-messenger observations with ET.

Estimates of the accuracy on cosmological parameters that can be obtained from bright sirens depend on the BNS and BHNS rates, which are currently less constrained than the BBH rate, and also on uncertainties on the network of electromagnetic observatories that will operate at the time of ET, as well as on the amount of telescope time that they will devote to the EM follow-up of GW events. Here we assume the two different scenarios for the joint GW+EM detection, already considered in [16]. In the first one, the merger of a BNS is followed by a Kilonova (KN) emission that is potentially observed electromagnetically by the Vera Rubin Observatory (VRO) [1162]. In the second scenario, under proper circumstances, a short Gamma Ray Burst (GRB) detection by THESEUS [1163, 1164] is associated to the GW event from a BNS. For the ET+VRO study we consider the multimessenger sources detected in one year of observations, while for ET+THESEUS, in order to have a statistically similar sample, we considers a 5 years catalog; the resulting dataset of bright sirens is the same as in tables 6 and 10 of [16]. We also use the same BNS population as in [16].[21]

As shown in [16] (see tables 28 and 29), the resulting marginalized error on H_0 in the GW+GRB case (and 5 yr of observations) is 5.7% for the 10-km triangle and 4% for 2L-15km-45° configuration, while for GW+KN (and 1 yr of observations) it is 0.9% for the 10-km triangle and 0.6% for 2L-15km-45°.

We have repeated the analysis showing also the impact of using the Planck 2018 [591] posterior distributions as a prior. The corresponding forecasts for the accuracy on H_0 and Ω_M are shown in figure 44 for GW+KN, and in 45 for GW+GRB. In particular, from these results we find that, when adding the Planck prior, the relative error on H_0 in the GW+GRB case (and 5 yr of observations) becomes 1.1% for both the 10-km triangle and for 2L-15km misaligned (so in this case the result is clearly dominated by the Planck prior), while for GW+KN (and 1 yr of observations) it becomes 0.7% for the 10-km triangle and 0.4% for 2L-15km misaligned.

We stress, however, that on top of the uncertainties related to the BNS rate and to the facilities and telescope time that will be available for the electromagnetic follow-up of GW events, the analysis performed in the GW+GRB case has been conducted under the assumption that the relative error on the luminosity distance can be approximated as 2/SNR, as assumed also in previous studies [16, 1165]. While the SNR^{-1} scaling theoretically represents a good

[21] This catalog is obtained from state-of-the art population models tuned to the O3 LVK data. The absence, to date, of BNS candidates in the currently ongoing O4 run implies that the rate used for BNS is now toward the upper range, rather than the mean value.

JCAP03(2026)081

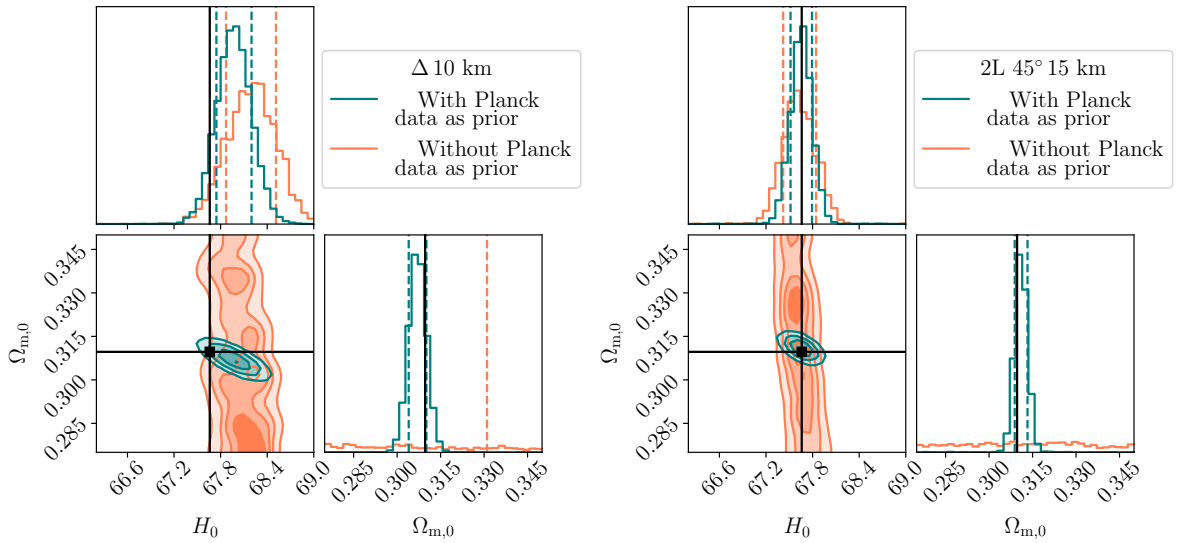

Figure 44. Results of the joint inference on the cosmological parameters H_0, $\Omega_{m,0}$, employing GW+KN events detected in one year of observations by the 10 km triangular (left panel) or the 2L-15km-45° (right panel) ET configurations, with the EM counterpart detected by the Vera Rubin Observatory. Vertical dashed lines represent the 68% CI of each distribution, while the black solid lines label the fiducial values.

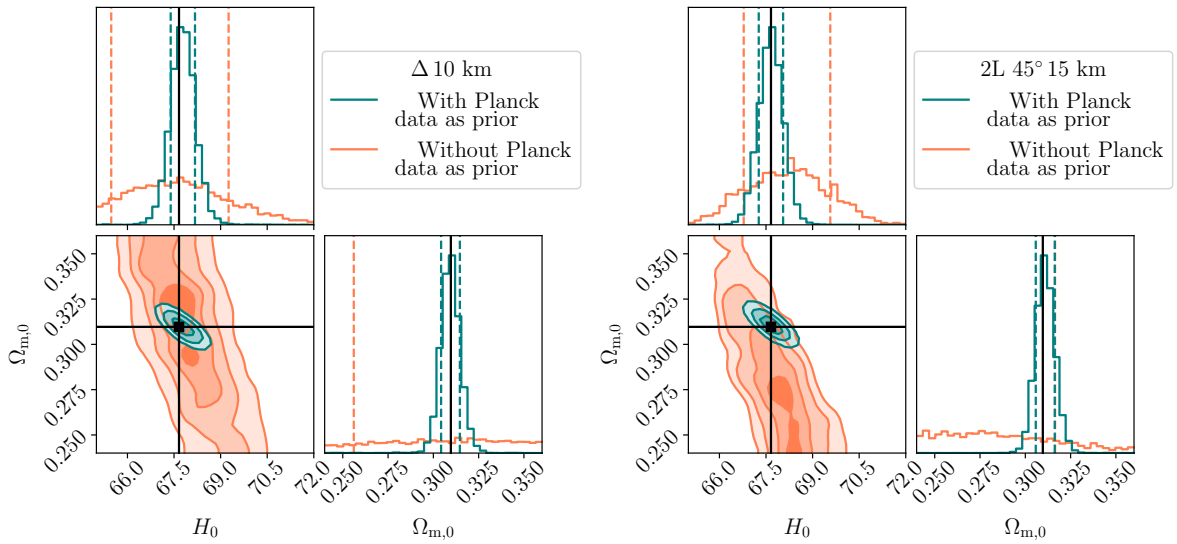

Figure 45. Results of the joint inference on the cosmological parameters H_0, $\Omega_{m,0}$ employing GW+GRB events detected in 5 years of observations by the 10 km triangular (left panel) or the 2L-15km-45° (right panel) ET configurations, with the EM counterpart detected by THESEUS. Vertical dashed lines represent the 68% CI of each distribution, while the black solid lines label the fiducial values.

JCAP03(2026)081

proxy for most of the parameter space, it reaches important limitations in some specific corners [1166]. In particular, the GRB counterpart associated to a GW event can be detected only for small inclination angles, since the emission mechanism typically ejects the material in the same direction of the angular momentum of the binary. This circumstance introduces two non-trivial challenges in the determination of the luminosity distance uncertainty: in the limit of face-on/face-off binaries, the Fisher Matrix becomes ill-conditioned, leading to an unfaithful reconstruction of the infamous d_L–ι degeneracy [1167, 1168] and to a regime where the 2/SNR approximation is not appropriate anymore; additionally, this intrinsic correlation gets stronger as the inclination angle approaches smaller values. The two above-mentioned effects, which inevitably appear in the framework of GW+GRB observations, represent non-negligible sources of bias that can jeopardize the whole inference if not taken into account for. A comprehensive description of how to properly deal with such issues has been recently proposed in [1169], where the Fisher Matrix limitations are overcome and the d_L–ι correlation is mitigated by the underlying fact that the EM detection implicitly select a specific corner of the parameter space, see also the discussion in section 10.2.3.

Besides model-based cosmological parameter estimation with bright sirens, one can also employ model-independent methods to reconstruct the distance-redshift relation and test for deviations of the standard cosmological model or some of its basic assumptions. That can be done for example with the use of Gaussian Process as in [1170–1172], or by combining GW distances with other distance indicators, such as standard candles and angular diameter distances from the large-scale structure [1172, 1173]. In ref. [1172], it was shown that fewer than 40 GW-GRB detections, in combination with forthcoming cosmological surveys, will enable unprecedented precision on H_0 and Ω_m, and accurately reconstruct the DE density evolution. Taking the ratio of different distances is an interesting approach as it avoids the intrinsic degeneracies present in the distance-redshift relation between standard cosmological parameters, notably Ω_m, and effects that can modify the GW luminosity distance or other cosmic distances, such as violations of the transparency of the Universe (cosmic opacity) or modified gravity (see section 3.3.2). In [1173], it was shown that, in combination with other distance measurements expected for the near future with surveys like Euclid, LSST, DESI and Roman, bright sirens from ET would allow tests of cosmic opacity together with deviations in the GW propagation due to modified gravity models that can be achieved with percent level precision, in various redshift bins up to $z = 0.9$, with no assumption on the redshift evolution of the mechanisms causing deviations from standard physics.

As shown in [1174], bright sirens will be useful tracers of both the density and velocity fields in cosmology. In particular, a combination of ET sirens with EM counterparts with LSST allows for a 30% improvement on the measurements of H_0 with ET alone, but also percent-level measurements of Ω_{k0} (an improvement of over one order of magnitude). We can also get good constraints on the growth of structure in particular on σ_8 and the growth-rate index γ. In [1174] it was also proposed the use of preliminary GW distances, obtained for the alerts for follow-ups, to inform the optimal telescope exposure time. It was shown that this technique reduces the necessary telescope time to obtain the same kilonova completeness by around 25%. This could be useful since in the ET era the bottleneck for bright sirens catalogs will possibly be due to available telescope time.

JCAP03(2026)081

3.3.1.2 Dark sirens. While bright sirens provide the most direct method of using resolved sources for late-time cosmology, the other side of the coin is the difficulty in the observation of the EM counterpart. Events with direct EM counterparts will constitute only a tiny fraction of the total detected events, with a strong selection from the EM side limiting these sources to redshifts generally of order $z \lesssim \mathcal{O}(1)$ [1165, 1175]. On the other hand, an unprecedented opportunity offered by ET will be the detection of compact binary mergers across all cosmic history, in particular BBH mergers up to redshift $\mathcal{O}(20)$ [16, 1167]. At redshifts below the star formation peak, ET can in particular detect almost 100% of the population [16, 1167]. The vast majority of these events will not have EM counterparts but contain precious information about the evolution of the Universe, especially at redshifts that are not accessible to the current generation of GW detectors, not even at their most advanced sensitivity. This will open a window on the evolution of the Universe well before the Dark Energy dominated era and beyond the star formation peak, possibly even in region where compact objects formed by standard stellar-evolution scenarios are expected to be absent [1176, 1177]. Even if their actual high-redshift nature will have to be carefully assessed on an event-by-event basis [1178–1181], inferring their statistical distribution might lead to clearer signatures [1182]. Therefore, methods that target the use of the full sample of detected events will be crucial for cosmography with ET. Several of those are actively being developed by the community, and are generally referred to as "dark siren" methods. The general principle behind dark sirens is the use of prior information on the properties of the underlying distribution of sources, of which the observed catalog is a biased sample, to break the degeneracy between source-frame masses and redshift in the GW waveform at the statistical level [1159].

The line-of-sight redshift prior. The GW observations provide a direct measurement of the luminosity distance. For a dark siren measurement of H_0 or the other cosmological parameters, the GW distance information needs to be convolved with some "prior" information on the redshift. This prior comes from the underlying cosmology and binary merger rate evolution (uniform part), as well as potential host galaxies (non-uniform part). Cosmology inference algorithms allow us to construct this prior along each line-of-sight. This line-of-sight redshift prior essentially consists of an in-catalogue part and an out-of-catalogue part. The in-catalogue part is constructed using redshifts and luminosities of the galaxies in the region. The luminosity (in a certain observation band) is used to effectively weight the galaxy in proportion to the probability of sourcing a merger. Astrophysical assumptions go into this construction, given that the luminosity in a certain band may trace a certain aspect of the astrophysics. The out-of-catalogue is used to model the galaxies which are beyond the catalogue, due to their distance or due to low intrinsic brightness. This part usually depends on galaxy luminosity parameters (or Schechter function parameters) in addition to the assumed cosmological model. A detailed prescription of the construction of the line-of-sight redshift prior can be found in [1161]. In the following paragraphs we describe the galaxy catalogs and surveys which can be used to construct this prior in the 3G era.

Galaxy catalogs. The lack of an EM counterpart poses a tough challenge in GW cosmology. However, as first proposed by Schutz in 1986 [1138], statistical approaches that rely on available galaxy catalogs can counterbalance the missing source's redshift information. Specifically,

JCAP03(2026)081

the potential host galaxies that fall in the localization error volume of a detected GW event display an inhomogeneous distribution that can be employed as redshift prior in the Bayesian framework. Contrarily to bright sirens, a single or few of such events are likely unable to deliver tight constraints on the cosmological parameters. As a statistical tool, the efficiency of this approach strongly relies on the size of the sample of dark sirens used, and we expect the precision to shrink with the square root of the number of events. In the past decade, this methodology has successfully been applied both to simulated [1142, 1145, 1147, 1160, 1183–1185] and real data with different galaxy catalogs, including GLADE/GLADE+ [9, 1143, 1161, 1186–1190], the Dark Energy Survey [1191, 1192], the DESI Legacy Survey [1193], the DECam Local Volume Exploration Survey [1194], DESI [1195], and to the PSZ2 and eRASS galaxy cluster catalogs [1196].

Spectral Sirens. A complementary possibility (also called the "spectral sirens" method) is the use of features in the source-frame mass distribution [1151–1156]. The population properties, in particular, the mass and redshift distributions, are given in source-frame; for example, one can predict the probability that a black hole has a certain mass, or forms at a certain redshift, from population synthesis codes [1197–1199]. On the other hand, GW detections measure detector-frame quantities (redshifted masses and luminosity distance). The population properties reconstructed in source-frame from detector-frame observations will thus be reshaped by a change of the cosmology. In case source-frame distributions are informative, the degeneracy between source-frame masses and redshift in the GW waveform can be broken by combining an ensemble of sources. This can drive constraints on cosmology, as the presence of preferential scales breaks the mass-redshift degeneracy at the statistical level.

Potential systematic effects. Recent advances have led to the development of pipelines incorporating information from both the mass distribution and galaxy catalogs [1147, 1160, 1161]. Thus one no longer needs to assume a fixed mass distribution for an inference using galaxy catalogs, which may otherwise have biased the measurement. Taking care of this leading order systematics exposes us to smaller sources of potential systematic uncertainties. These can come from the GW data, the EM data, or the underlying assumptions. It is crucial to understand and address even the smallest of the potential systematic effects as the statistical power of the data increases, in order to converge towards an unbiased measurement. On the GW side, mis-modelling the source population or its redshift evolution could pose a problem [1200]. On the EM side, it is important to understand redshift measurement errors [1201]. Uncertainties in the measurement of galaxy luminosities and the measurement of the Schechter luminosity function parameters (and their evolution) come next [1202]. It has recently been shown that the results could be biased due to incorrect assumptions on the luminosity weighting of galaxies [1203, 1204]. A large body of work is underway largely in the context of upcoming LVK observations [1205], to understand and address small systematic effects and ensure an accurate measurement as we move towards precision. Targeted studies to determine the potential of these techniques for ET will be necessary in the future.

The 3G era is expected to bring $\mathcal{O}(10^{4-5})$ BBH detections per year. Albeit computationally challenging, this abundance naturally meets the conditions that make the galaxy catalog approach a powerful statistical tool. Indeed, current forecasts predict that a sub-percent

JCAP03(2026)081

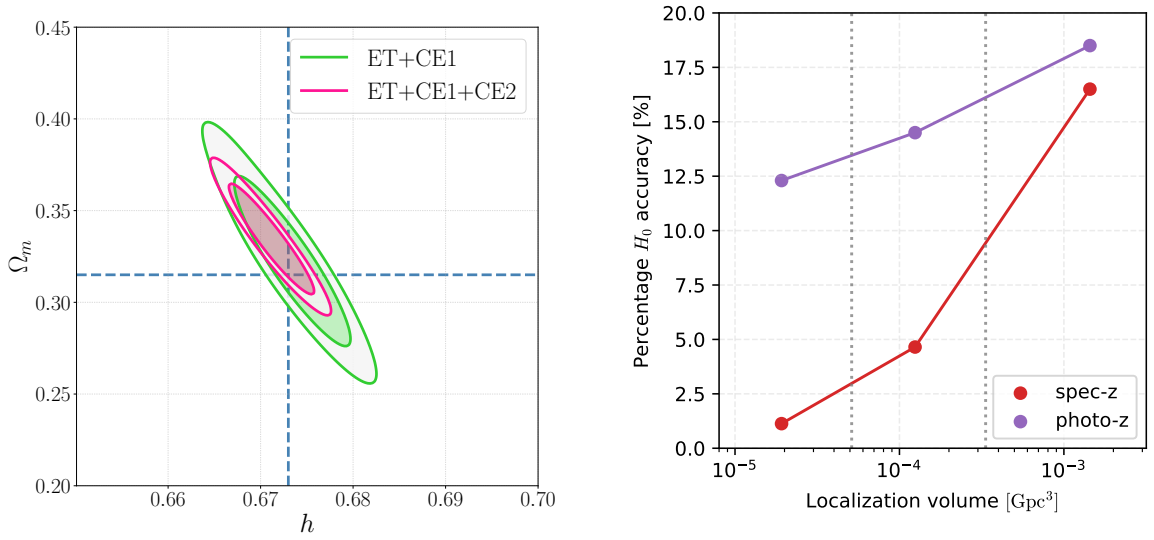

Figure 46. *Left panel:* posterior joint distribution on H_0 and $\Omega_{\mathrm{m},0}$ obtained by employing BBHs as dark sirens and cross correlating the loudest GW event localization volumes with a galaxy catalog. The contours, which refer the 68% and 90% confidence level, are shown for two networks of 3G detectors assuming one year of continuous observations. Here ET is in a 10 km-triangular configuration and CE1 and CE2 correspond to 40 km and 20 km Cosmic Explorer, respectively. Reprinted figure with permission from [1185], copyright (2023) by the American Physical Society. *Right panel:* dependence of the accuracy on H_0 on the GW event localization volume with a photometric (`photo-z`) or spectroscopic (`spec-z`) galaxy catalog.

measurement of H_0 and a $\sim 10\%$ measurement of $\Omega_{\mathrm{m},0}$ can confidently be attained by 3G detectors by employing only the loudest dark sirens observed in one year [1185, 1206]. Yet, as shown in figure 46, reaching this precision requires a mandatory joint effort between more than a single 3G detector, as the localization power plays a crucial role in the statistical machinery.

We stress, however, that these predictions are subject to variability, which depends on the properties of the galaxy catalog adopted in these studies. A promising candidate will be the database created from the observations of the Vera Rubin Observatory. It is predicted to contain 10^{10} galaxies up to a redshift $z \leq 6$, covering 20,000 square degrees. For about 4×10^9 galaxies, six-band photometric measurements and shape measurements will be available, making the estimation of photometric redshifts much more precise [1207]. Early estimations show that a faint sample of all types of galaxies having photometric information in 6 bands would have a statistical photo-z error of $\Delta z \sim 0.05\,(1+z)$ per galaxy [1208]. Even assuming improved photometric redshift estimating techniques, the errors from these measurements would be an important source of uncertainty for the dark siren results. As demonstrated in [1147], the accuracy in redshift determination plays a crucial role in the estimate of cosmological and astrophysical parameters, since already at O5 sensitivities the accuracy on the determination of H_0 can improve down to the percent level when a spectroscopic catalog is considered (see figure 46, right panel). Hence, a spectroscopic survey would be crucial to maximising the potential of this method.

JCAP03(2026)081